energies

MDPI

Article

Enhancing Reservoir Simulation History Matching Using SHAP Value for Parameter Range Selection

Grachik Eremyan, Adel M. Magdeev, Mohammed Al-Shargabi, Ivan V. Matveev, Ivan E. Smirnov, Gleb Y. Shishaev and Shadfar Davoodi *

School of Earth Sciences & Engineering, National Research Tomsk Polytechnic University, 30 Lenin Avenue, 634050 Tomsk, Russia; eremyanga@hw.tpu.ru (G.E.); amm43@tpu.ru (A.M.M.); al_shargabi@tpu.ru (M.A.-S.); matveeviv@hw.tpu.ru (I.V.M.); smirnovie@hw.tpu.ru (I.E.S.); shishaevgy@hw.tpu.ru (G.Y.S.)
* Correspondence: davoodis@hw.tpu.ru

Abstract

Accurate reservoir history matching is indispensable for reliable subsurface forecasting and optimal field development; however, it remains a formidable challenge due to the high dimensionality of geological parameter spaces, strong nonlinear dynamics, and the competing demands of computational efficiency and data fidelity. Conventional automated history matching workflows frequently rely on Tornado sensitivity analysis, which evaluates parameters in isolation and fails to capture critical interdependencies that govern reservoir response, leading to inefficient exploration and suboptimal convergence. This study, therefore, introduces a novel Shapley Additive Explanations (SHAP)-assisted adaptive history matching framework that integrates SHAP with a CatBoost (v1.0.0) regressor to enable quantitative, model-agnostic assessment of parameter contributions while explicitly resolving non-linear feature interactions unattainable with conventional methods. The workflow establishes a systematic methodology for refining parameter uncertainty ranges prior to optimization through SHAP dependence plots, which identify subspaces where the objective function decreases, yielding 25–68% range reductions across all cases without compromising geological plausibility. Both SHAP-assisted and Tornado-based workflows, coupled with identical Particle Swarm Optimization settings, are rigorously validated on two synthetic reservoirs (SRM-6, Egg) and a real Siberian field case. Results demonstrate that the SHAP-assisted approach achieves equivalent or superior history match quality while reducing required optimization cycles by 6–60%, depending on model complexity, delivering lower objective function values and improved alignment with observed data. Computational efficiency is further enhanced by reusing the Latin Hypercube Sampling dataset for surrogate training, sensitivity analysis, and range refinement, contrasting sharply with Tornado's requirement for 2N + 1 dedicated simulation runs with limited reusability. This framework advances interpretable, data-driven history matching by providing engineers with a systematic method to prioritize calibration efforts, reduce computational burden, and improve forecast reliability in complex reservoir systems.

Keywords: Shapley Additive Explanations analysis; CatBoost regression; history matching; reservoir simulation; uncertainty quantification

Check for updates

Academic Editor: Tarek Arabi Ganat

Received: 27 March 2026
Revised: 4 May 2026
Accepted: 6 May 2026
Published: 9 May 2026

Copyright: © 2026 by the authors. Licensee MDPI, Basel, Switzerland. This article is an open access article distributed under the terms and conditions of the Creative Commons Attribution (CC BY) license.

1. Introduction

Reservoir simulation is a cornerstone of modern reservoir management, enabling replication of field conditions through geological models, petrophysical properties, fluid

saturations, relative permeability functions, and well specifications [1]. It provides integrated static (geological) and dynamic representations of reservoir performance [2]. Reflecting its growing industrial importance, the worldwide reservoir analysis market is anticipated to expand from $9.63 billion in 2024 to $13.72 billion by 2029 [3]. A key advantage lies in forecasting production and pressure trends; however, such predictions require rigorous calibration. First, simulation models must be history-matched to consider uncertainties and reproduce historical data [1,4]. Second, without an adequate match to past performance, reliable future forecasts cannot be achieved. In practice, achieving such calibration is challenging because modern reservoir models still contain a large number of uncertain parameters whose combined effects are highly nonlinear [5,6]. As a result, the central challenge in reservoir model calibration is the inefficient exploration of high-dimensional uncertain parameter spaces during assisted or automated history matching (AHM) [1,2]. This inefficiency stems from conventional sensitivity analysis methods, such as the Tornado approach, which assume parameter independence and linear response, ignoring nonlinear interactions that dominate real reservoir dynamics [7]. Consequently, these methods misidentify influential parameters and mandate overly conservative uncertainty bounds, forcing optimizers to evaluate vast, irrelevant regions of the search space. This dramatically increases computational cost while yielding suboptimal matches, a fundamental limitation in industrial workflows [8]. History matching (HM) is thus essential for calibrating reservoir simulation models (RSMs) against field observations [4,9], involving adjustment of input parameters to align simulated outputs with measured performance. Accurate HM improves reservoir understanding, optimizes development strategies, and enhances confidence in future predictions aligned with business objectives [1,10]. Currently, model calibration follows two main approaches: manual adjustment by expert reservoir engineers and AHM. In manual HM, experts select parameters deemed reasonable based on domain knowledge and experience [5,6]. Consequently, this method relies on the assumption that the deterministic model provides a reliable representation of the reservoir, an assumption that is intuitive but not always valid. Manual HM is time-consuming and resource-intensive, heavily dependent on human expertise [1,5,6]. In contrast, the development of AHM methodologies directly addresses these limitations through algorithmic parameter optimization. The effectiveness of both manual and AHM approaches is often limited by the large number of uncertain parameters in the model, which determines the complexity of its configuration and significantly increases the computational requirements for comprehensively exploring the solution search space. Therefore, various AHM methods have been developed to overcome these problems, such as parameter clustering [4], model zoning [11], local parameterization [12,13], surrogate modeling (proxy modeling), and other methods aimed at simplifying the computational process, increasing the accuracy and efficiency of HM [14,15]. As an inverse problem, HM admits multiple combinations of control parameters that can lead to similar production responses. In this context, the role of optimization becomes central [16]. AHM leverages optimization algorithms to automatically identify model parameters that minimize the objective function (OF) [16]. Formulating the OF is the first step, followed by applying optimization algorithms to identify parameters that minimize the mismatch. The success of this process hinges critically on the selected optimization strategy [15]. Over recent decades, AHM optimization algorithms have evolved into four principal categories: gradient-based methods, global optimization algorithms, data assimilation techniques, and reinforcement learning approaches [15], as illustrated in Figure 1.

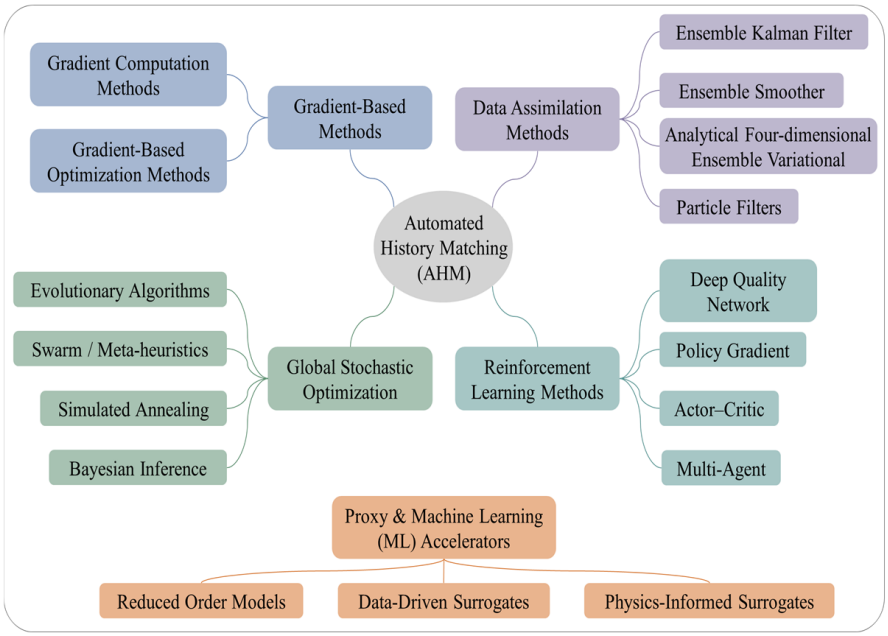


Figure 1. Overview of automated history matching (AHM) approaches. The diagram condenses AHM into four well-established algorithm families—gradient-based, global stochastic, data assimilation, and reinforcement learning—while emphasizing that proxy and machine learning (ML) accelerators act as cross-cutting speed-up tools rather than stand-alone optimization strategies.

Additionally, prevalent HM techniques include evolutionary algorithms, particle swarm optimization (PSO), and proxy-based methods [16,17]. Gradient-based methods efficiently handle smooth, continuous, differentiable OFs, converging quickly to local optima [16,18,19], but they falter on non-linear or discontinuous problems and often get trapped in local minima, missing the global optimum [16]. Evolutionary algorithms, inspired by biological evolution, evolve solutions via selection, mutation, and crossover [16]; for example, differential evolution is simple yet performance-sensitive to control parameters, while advanced variants like hybrid differential evolution and distributed surrogate systems improve efficiency for complex AHM tasks [15]. Surrogate models approximate full-physics reservoir simulations, enabling rapid OF evaluation and drastically reducing computational cost [20], though their success hinges on accurately capturing the reservoir's non-linear, dynamic behavior. Currently, diverse optimization algorithms are employed in HM, each suited to different problem complexities [21]; among them, PSO is noted for its simplicity and robustness in solving non-linear, non-convex problems [22] and for showing faster convergence in low-dimensional cases [21]. This efficiency has driven PSO's widespread use in modern reservoir simulation [23,24], including its integration into the software used here, and it remains amenable to improvement through adaptive parameterization. Furthermore, PSO yields HM results comparable to the Ensemble Kalman Filter and consistently outperforms the Genetic Algorithm in convergence speed [21,25]. AHM workflows remain fundamentally constrained by the quality of the initial parameter-screening stage. If the uncertainty ranges provided to the optimizer are overly broad or include weakly influential parameters, even the most sophisticated optimization algorithms expend substantial computational effort exploring unproductive regions of the search space. Thus, the critical unresolved problem in industrial AHM practice lies not in optimization itself, but in the lack of reliable pre-optimization insight into which uncertain parameters, and parameter interactions, truly control the OF. Existing optimization and data-assimilation methods cannot resolve this issue because they operate only after the parameter space has been defined. Consequently, improvements in optimization strategy

alone cannot compensate for inadequate parameter screening. The motivation of this work is therefore to address this gap by introducing a systematic, data-driven, and interpretable pre-optimization framework for AHM. Accordingly, the primary research question of this study is formulated as follows: Under strictly identical reservoir modeling conditions and optimization settings, does the integration of a SHAP-based pre-optimization framework systematically accelerate convergence and improve the final history-match quality compared to the conventional Tornado-based approach? To address this, the testable hypothesis is that utilizing SHAP value analysis (extracted via a CatBoost surrogate trained on an initial Latin Hypercube Sampling dataset) to capture non-linear parameter interactions and refine uncertainty ranges will focus the search space on highly productive sub-spaces prior to optimization. Assuming ceteris paribus conditions—employing the exact same PSO algorithm, identical hyperparameter settings, and the same initial reservoir models and uncertainties—the proposed SHAP-assisted workflow will require fewer optimization cycles to converge and will yield an ensemble of history-matched models that more accurately reproduces historical production data than the conventional workflow. To evaluate this hypothesis, both workflows are rigorously compared using three specific performance criteria: (1) the quantifiable percentage reduction in the initial parameter uncertainty ranges prior to optimization; (2) the computational efficiency gained, measured by the reduction in the number of required optimization cycles (PSO generations) to achieve convergence; and (3) the comparative quality of the final history match, assessed through the absolute reduction in the global objective function (GOF) values and the visual fidelity of alignment with historical production data. Recent advances in ML and artificial intelligence (AI) have indeed opened new opportunities for improving the HM process [16], enabling faster navigation of complex, high-dimensional parameter spaces. However, many of these methods operate as "black boxes", providing limited insight into how predictions are generated [26] and, depending on configuration, potentially incurring significant computational overhead [27]. This lack of interpretability poses a critical barrier to ML adoption in reservoir engineering, where decisions rely heavily on domain knowledge and trust in model behavior [27]. Among ensemble ML methods, CatBoost has recently attracted attention for its strong performance on small and noisy datasets, characteristics typical of reservoir engineering data [28]. CatBoost natively handles categorical features and mitigates overfitting through ordered boosting and symmetric tree construction [28], features that contribute to its consistently strong performance in practical applications. In pressure forecasting and oil production modeling, CatBoost has been shown to outperform other gradient boosting algorithms in terms of prediction accuracy and robustness while also demonstrating lower variance and superior generalization [29,30]. These characteristics make CatBoost a suitable candidate for HM applications, especially when the available dataset is sparse or heterogeneous [31]. However, predictive accuracy alone does not resolve the core AHM challenge of parameter screening. While powerful on its own, CatBoost's true potential in AHM is realized when coupled with Shapley Additive Explanations (SHAP), not as a post hoc diagnostic, but as a pre-optimization scoping tool that directly addresses the limitations of Tornado analysis. SHAP is rooted in cooperative game theory, which distributes the "contribution" of each player (in this case, an HM parameter) to the final result (OF value) [32]. By capturing both individual and interaction effects, SHAP provides a transparent, model-agnostic interpretability framework [33]. Unlike conventional sensitivity analysis, SHAP enables systematic identification of influential parameters and nonlinear interactions using only simulation outcomes [34]. When applied prior to optimization, this information enables informed refinement of uncertainty ranges and exclusion of weakly influential parameters, transforming AHM from a brute-force exploration into a focused, information-driven process.

Therefore, the present study investigates the application of SHAP analysis using the CatBoost regressor within the AHM framework to gain deeper insights into parameter sensitivities, enhancing the efficiency and accuracy of the HM process by leveraging model-agnostic explanations to identify the most influential input parameters. Unlike conventional Tornado sensitivity, this approach enables quantitative assessment of parameter contributions to the objective function while capturing non-linear interdependencies and local feature dependencies. A systematic, data-driven methodology for refining parameter uncertainty ranges prior to optimization is implemented using SHAP dependence plots, which identify subspaces where the objective function decreases, thereby reducing parameter ranges across all models and focusing the search space without sacrificing physical plausibility. The approach is validated through two synthetic reservoir models, namely, the SRM-6 [35] and the Egg model [36], as well as a real-world Siberian reference (SR) field, demonstrating its effectiveness in both controlled and practical cases.

2. Methodology and Theory

This study integrates ML with interpretable artificial intelligence (SHAP) to identify the most influential parameters and reduce uncertainty ranges prior to optimization, thereby decreasing the number of required AHM iterations and improving objective function convergence. Figure 2 outlines the four-stage comparative framework for evaluating conventional and SHAP-assisted AHM-WFs.

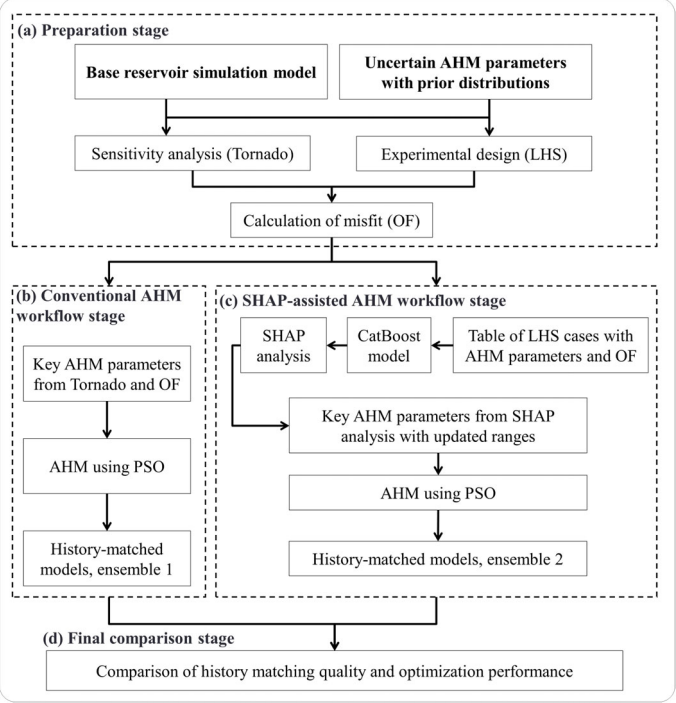


Figure 2. Comparative design of conventional and SHAP-assisted/automated history matching workflows (AHM-WF). Key stages include: (**a**) Preparation stage: both WFs start from a base reservoir model and uncertain AHM parameters with prior ranges and distributions; Tornado sensitivity analysis and Latin Hypercube Sampling (LHS) are performed separately, followed by objective function (OF) evaluation. (**b**) Conventional AHM stage: key parameters selected via Tornado and OF rankings are optimized with Particle Swarm Optimization (PSO) to produce Ensemble 1. (**c**) SHAP-Assisted AHM stage: an LHS-generated dataset (parameters and OF values) trains a CatBoost model; SHAP analysis refines parameter uncertainty ranges, and PSO is initialized to yield ensemble 2. (**d**) Comparison stage: ensembles 1 and 2 are compared to assess gains in history match quality and optimization performance, particularly in convergence speed and solution accuracy.

The methodology begins with the definition of a base RSM and the specification of uncertain AHM parameters along with their prior ranges and probability distributions. In the second stage, two parallel WFs are initiated. The conventional AHM-WF employs Tornado-based sensitivity analysis to rank parameter influence, followed by selection of key parameters based on combined Tornado and OF misfit results; HM is then performed using PSO, yielding the 1st history-matched ensemble (Ensemble 1, see Sections 2.2.1 and 2.2.2). Concurrently, the SHAP-assisted WF generates a training dataset via Latin Hypercube Sampling (LHS), computes the OF for each sampled simulation case, and constructs a tabulated dataset of input parameters and corresponding misfit values. This dataset is used to train a CatBoost regressor, on which SHAP value analysis is subsequently applied to quantify parameter contributions and refine uncertainty ranges for the most influential parameters (see Section 2.2.3). The third stage implements PSO-based HM utilizing the revised AHM parameter ranges obtained from SHAP analysis, generating a history-matched ensemble (Ensemble 2) with the same PSO hyperparameters as those used in the conventional WF (see Sections 2.2.4 and 2.2.5). The fourth stage involves a quantitative comparison of the two ensembles in terms of HM quality (e.g., reduction in absolute OF values, data alignment) and optimization performance (e.g., convergence rate, stability). The final stage evaluates the added value of SHAP-guided parameter refinement by assessing improvements in solution accuracy, computational efficiency, and robustness of the HM process, thereby validating the proposed SHAP-assisted AHM framework against conventional practice through rigorous quantitative comparison of HM quality, convergence behavior, and computational efficiency across multiple reservoir models.

To ensure full reproducibility of the proposed methodology, the exact procedural sequence of model generation, surrogate training, parameter screening, and optimization is formalized in Algorithm 1.

Algorithm 1: Procedural sequence of the comparative AHM framework

Input: Base Reservoir Simulation Model, Historical production data.
Output: History-matched Ensembles (1 and 2), comparative convergence metrics.
Phase 1: Initialization
1: Define N uncertain AHM parameters $X = \{x_1, x_2, ..., x_N\}$ along with their prior ranges $[X_{min}, X_{max}]$ and probability distributions.
Phase 2: Parallel Pre-Optimization (Parameter Screening & Range Refinement)
Path A: Conventional AHM workflow
2: Generate 2N + 1 simulation models varying one parameter at a time.
3: Execute simulator runs and compute the OF for each case.
4: Rank parameters using a Tornado chart and select the key influential parameters.
Path B: SHAP-assisted AHM workflow
5: Generate M experimental models using LHS.
6: Execute M simulator runs and compute the OF for each case.
7: Train a CatBoost regressor $f(X) \approx$ OF using an 80/20 train-test split and grid search hyperparameter tuning (as detailed in Section 2.2.3).
8: Compute SHAP values for the dataset to evaluate marginal feature contributions and non-linear interactions.
9: Rank parameters by mean absolute SHAP value and select the most influential ones.
10: Refine parameter ranges to $[X_{min}', X_{max}']$ by isolating continuous sub-spaces where SHAP values are consistently negative (indicating OF reduction).
Phase 3: History Matching (Optimization)

Algorithm 1: *Cont.*

11: Initialize PSO under identical configurations (swarm size, inertia, sociality, and matched random seeds across respective runs).
12: For Path A: Execute PSO within initial ranges [X_{min}, X_{max}] for parameters selected in Step 4 → Generate Ensemble 1.
13: For Path B: Execute PSO within refined ranges [X_{min}', X_{max}'] for parameters selected in Step 9 → Generate Ensemble 2.
Phase 4: Evaluation
14: Compare Ensemble 1 and Ensemble 2 based on convergence speed, absolute OF reduction, and historical data alignment.

2.1. Data Collection, Preparation, and Reservoir Modeling

In this subsection, the initial data, uncertain parameters, and their prior ranges are established for all three models. It is important to emphasize that the primary scope of this study is the comparative evaluation of the optimization workflows rather than the geological justification of the reservoir models themselves; therefore, the uncertain parameter spaces are treated as established inputs. For the synthetic models (SRM-6 and the Egg model), sets of 8 and 11 key HM parameters were established a priori, respectively. These prior ranges were derived from their original benchmark specifications [35] and intentionally supplemented by engineering judgment, e.g., introducing petrophysical consistency and anisotropy in the Egg model, to ensure a highly non-linear and challenging search space suitable for rigorous AHM algorithm testing (see Sections 2.1.1 and 2.1.2). For the SR field, a comprehensive initial set of 255 uncertainties was identified and parameterized by a cross-functional team of geoscientists and reservoir engineers. As detailed in Section 2.1.3, these prior ranges were derived directly from real field knowledge, including seismic interpretations, well logs, and core analyses from 13 exploration wells, and were carefully supplemented by expert judgment in areas characterized by data scarcity.

Furthermore, for both synthetic reservoir models (SRM-6 and the Egg model), the selected grid resolutions and block dimensions are strictly based on their established benchmark designs. These grid configurations were specifically validated during their original development to ensure numerical stability and mitigate the effects of numerical dispersion. This guarantees that the variations in the objective function observed during the optimization process reflect true parameter sensitivities rather than numerical artifacts, thereby ensuring the reliability and generalizability of the history-matching conclusions.

2.1.1. Synthetic Reservoir Model: SRM-6

SRM-6 is a synthetic reservoir model intersected by a fault, featuring a six-well configuration (three injectors and three producers) [35]. This numerical model employs a Cartesian grid of 18 × 24 × 15 cells (totaling 6480 cells), covering an area of 1800 × 2400 m with a net pay thickness of 11–14 m. The model simulates a waterflood development with seven years of production history and is well-suited for numerical experiments due to its synthetic nature. The corresponding matching parameters are summarized in Table 1. All parameters correspond to the type "*real*" and have a *uniform* distribution. These parameters were selected based on their significant influence on the reservoir model's fluid flow behavior, ensuring that the HM process effectively captures key dynamic responses. Base values represent initial estimates, while true values reflect actual properties used to generate synthetic production data; further details on the SRM-6 model are provided in the original reference [35].

Table 1. History matching (HM) parameter ranges and base/true values for the synthetic reservoir model (SRM-6).

HM Parameter Description	Designation	Min	Max	Base	True
Free water level depth, m	FWL	2445	2455	2453	2450
Corey exponent of relative permeability for oil	N_o	3.0	8.0	3.3	5.0
Corey exponent of relative permeability for water	N_w	0.6	5.0	3.0	1.2
Water relative permeability at residual oil saturation	K_{rw_Sorw}	0.3	0.9	0.4	0.7
Coefficient "a" in the exponential porosity–permeability equation	K_A	64	74	68	70
Coefficient "b" in the exponential porosity–permeability equation	K_B	8.0	9.0	8.6	8.2
Vertical permeability anisotropy coefficient	K_v/K_h	0.01	0.30	0.02	0.20
First coefficient in the natural logarithmic water saturation-J-function equation	SW_A	−0.20	−0.14	−0.15	−0.18

2.1.2. Synthetic Reservoir Model: The Egg Model

The base Egg Model dataset, originally introduced by Jansen in 2014 [36], serves as a widely accepted benchmark for studies in computer-assisted flood optimization and HM. The model consists of 18,553 active grid cells and represents a five-spot field development scheme with eight injection and four production wells. The initial porosity cube was assigned a constant value of 0.2 throughout the model. Several modifications were introduced to improve geological consistency and ensure stable, reliable simulation results. The permeability cube exhibits a distribution typical of fluvial channel depositional environments. To reflect the expected petrophysical relationship, the porosity cube was recalculated from the initial horizontal permeability cube, preserving the same average porosity and original hydrocarbon in place. During AHM, the permeability field was varied using the porosity–permeability relationship. Additional XY-direction anisotropy was introduced to better capture fluid flow behavior in channelized settings. Corey-type relative permeability endpoints and exponents were also adjusted to minimize deviations in production profiles. Historical production data, including oil and water production rates, water injection rates, and bottom-hole pressures, were generated from the modified RSM under bottom-hole pressure control. The resulting hydrodynamic calculations were treated as historical data. The true HM parameters that reproduce these production behaviors are listed in Table 2. All parameters are of type "*real*" and follow a *uniform* distribution. In the Egg Model, these variables strongly influence fluid flow and saturation behavior. The base values serve as initial guesses in the HM process, while the true values represent the actual properties used to generate the synthetic data; further details on the Egg model are provided in the original reference [36].

Table 2. History matching (HM) parameter ranges and base/true values for the synthetic reservoir model (Egg model).

HM Parameter Description	Designation	Min	Max	Base	True
Coefficient "a" in the exponential porosity–permeability equation	K_A	54.0	61.0	57.5	54.509
Coefficient "b" in the exponential porosity–permeability equation	K_B	4.6	6.0	5.3	4.662
Permeability anisotropy coefficient in XY direction	K_x/K_y	0.50	1.00	0.75	0.75
Vertical permeability anisotropy coefficient	K_v/K_h	0.1	0.5	0.3	0.3
Critical water saturation	SWCR	0.10	0.16	0.13	0.132
Residual oil saturation	SOWCR	0.16	0.30	0.23	0.252
The relative phase permeability of oil with residual water saturation	KROLW	0.8	1.0	0.9	0.9
The relative phase permeability of oil with critical water saturation	KRORW	0.50	0.80	0.65	0.796
The relative phase permeability of water with residual oil saturation	KRWR	0.50	0.80	0.65	0.517
The degree of Corey for the relative phase curve of oil	N_o	2.5	5.5	4.0	2.567
The degree of Corey for the relative phase curve of water	N_w	1.5	4.5	3.0	3.892

2.1.3. Siberian Reference Field Real-World Case Study

The Siberian reference (SR) field, located in Western Siberia, hosts hydrocarbon accumulations associated with the Vasyugan Suite, with primary reservoirs of the Jurassic period. Within the field, multiple accumulation types have been identified, including oil-bearing and water-saturated zones developed in sandstones interbedded with clay lenses. Seismic interpretation is subject to considerable uncertainty arising from localized phase losses, which reduce the reliability of mapping seismic reflectors and stratigraphic horizons. The structural framework of the field is highly complex, influenced by an extensive system of faults and dislocations that subdivide the reservoir into four discrete structural blocks. Figure 3 depicts the structural map of the SR field alongside the schematic cross-section of Jurassic formations (J) from J1 to J4.

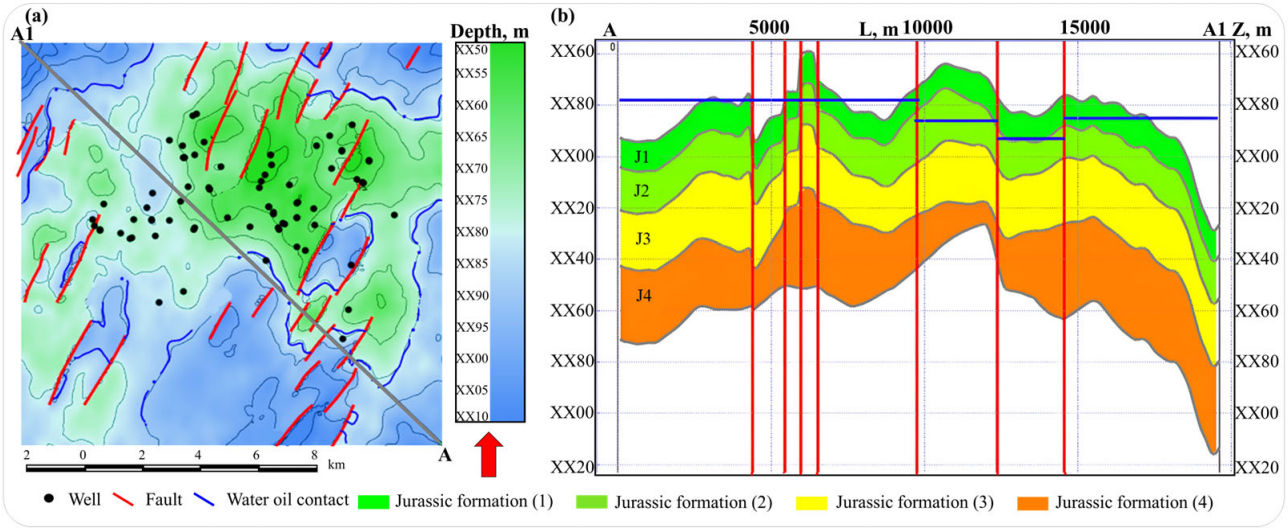


Figure 3. Structural characteristics of the Jurassic reservoir in the Siberian reference (SR) field: (**a**) Structural map at the top of the Jurassic formations (J1), showing wellhead locations (black dots), fault trace (red line), oil–water contact (blue line), and cross-section line A–A1 (gray), the red arrow indicates the direction to the north. (**b**) Geological cross-section along A–A1, illustrating fault segmentation into discrete blocks, each with independent oil–water contacts (blue) and fault seals (red), controlling fluid distribution and trap integrity. The actual information regarding the figure has been anonymized because of the data confidentiality constraints set by the partner company.

The characterization of petrophysical relationships, such as porosity–permeability dependencies and J-function–water saturation equations, is further complicated by significant heterogeneity, primarily due to tectonic deformations and associated lithological variability. Key subsurface uncertainties include the precise depths of fluid contacts within each block, the transmissibility of fault zones, relative phase permeabilities, capillary pressure functions, and the spatial extent of transition zones within the reservoir [37–39].

Table 3 summarizes the HM parameters identified during the analysis of the raw field dataset. Additionally, the degree of aquifer support remains undetermined, which is a critical variable for evaluating the reservoir's energy regime and potential production performance. The analyzed well inventory consists of 47 deviated wells, 26 horizontal wells, and 13 exploration wells with core acquisition, including both standard and specialized core analyses.

Table 3. History matching (HM) parameters for the Siberian reference (SR) field, categorized by reservoir modeling group, showing the number of adjustable parameters and their assigned prior probability distributions.

Modeling Section (Characteristics)	Number
Structural surfaces	3
Qa1zsss	19
Reservoir porosity	1
Reservoir permeability	61
Fault conductivity	27
Fluid contacts	4
Irreducible water saturation	2
Water saturation in the transition zone	24
Relative permeability parameters	111
Critical water saturation	1
Critical oil saturation	1
Aquifer size	1
Total number of HM parameters	255

2.2. History Matching Workflow and Model Calibration

Following the description of the synthetic models (SRM-6 and Egg models) and the SR field parameters, this subsection details the establishment of the conventional and SHAP-assisted AHM-WFs. This was accomplished by defining a base reservoir model and prior uncertainty ranges for the HM parameters. Subsequently, a Tornado-based sensitivity analysis was performed to exclude non-influential parameters from optimization (see Section 2.2.1). An OF was formulated to quantify mismatches between observed and simulated production data, with term-specific weights calibrated to ensure balanced contributions across all wells, time steps, and data types (see Section 2.2.2). A CatBoost regressor was then trained to emulate the simulator response efficiently (see Section 2.2.3), and SHAP-based interpretability was applied to rank parameter importance, capture interdependencies, and refine uncertainty ranges using a Latin Hypercube Sampling dataset (see Section 2.2.4). Finally, PSO was deployed with identical hyperparameters across both WFs to minimize the objective function, enabling a fair comparison between the conventional and SHAP-assisted strategies (see Section 2.2.5).

2.2.1. Objective Function Formulation

The objective function (OF) is a measure of the mismatch between observed and simulated production data. It quantifies the difference between observed and simulated values across multiple time steps, wells, and components (terms). The capability of the OF formulation used in this study is evidenced by its ability to achieve reliable convergence and balanced performance [35,40,41]. Moreover, it reduces the impact of data noise through normalized weighting and supports stable, efficient optimization by maintaining a well-conditioned structure [35,41]. The global OF (GOF) is calculated as:

$$GOF = \sum_{term} \frac{W_{term}}{\sum_{term} W_{term}} \cdot \left(\frac{W_{obj}}{\sum_{obj} W_{obj}} \cdot \sqrt{\frac{\sum_{n=k}^{N} W_n \cdot \left(\frac{value(O) - value(S)}{g} \right)^2}{\sum_{n=k}^{N} W_n}} \right) \quad (1)$$

where W_{term} is the weight assigned to a specific term; W_{obj} denotes the weight of the object (e.g., well or group) corresponding to that term; W_n is the weight associated with time step n; value(O) and value(S) are the observed and simulated values, respectively;

and g is the absolute error tolerance, defined as 1 sm^3 for liquid rates, 1 bar (absolute) for pressures, and 1000 sm^3 for well gas production rates in the SR field model. In the synthetic models SRM-6 and Egg, the GOF in the form of the root mean square error (RMSE) includes the following terms: well oil production rate (WOPR), well water production rate (WWPR), well water injection rate (WWIR), and well bottom-hole pressure (WBHP). The weights for these terms were calculated to be inversely proportional to average historical oil production rates, taking into account absolute measurement error [42]. Every object (well) has an equal weight (1) in each term. In the SR field model, the GOF was derived from the previous terms by integrating the well gas production rate (WGPR) and the average reservoir pressure within the 3 × 3 cell block centered on the well, referred to as WBP9, in the hydrodynamic simulation. Term weights were allocated inversely proportional to their discrepancies concerning the overall goodness of fit, thereby equilibrating contributions despite variations in absolute mismatch values. Figure 4 depicts the application of the Latin Hypercube Sampling (LHS) dataset for assessment, guaranteeing that each term's contribution to the overall GOF value was roughly equivalent. The weights of the objects (wells) were computed using a methodology analogous to that employed in synthetic reservoir models [42]. The weights assigned to each model are presented in Table 4.

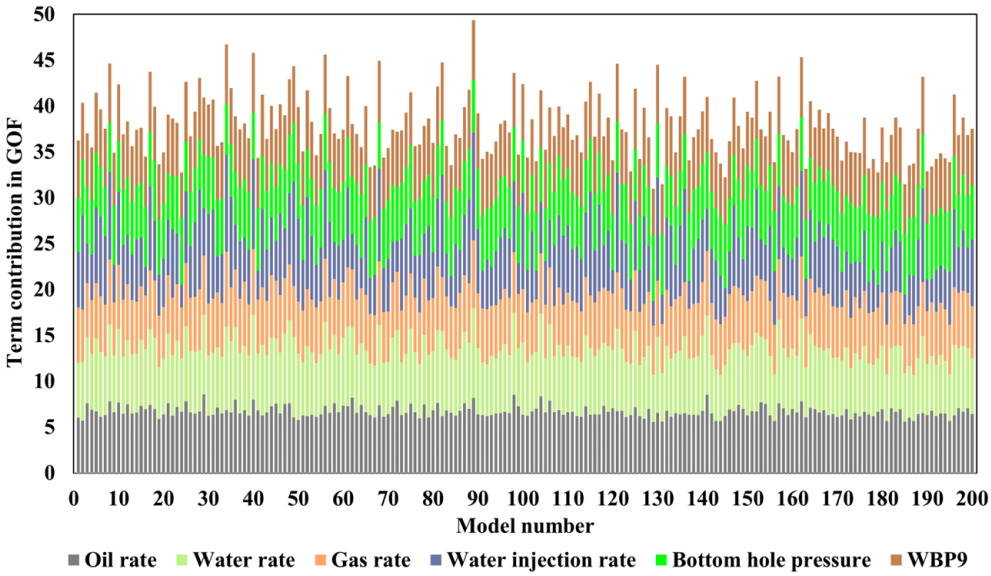


Figure 4. Contribution of each individual HM term (oil rate, water rate, gas rate, water injection rate, bottom hole pressure, and the average reservoir pressure in the 3 × 3 cell block centered on the well (WBP9)) to the total global objective function (GOF) value for each model in the Latin hypercube sampling dataset. The weights for each term were calibrated to ensure their contributions were approximately equal prior to the main history matching (HM) process.

Table 4. Summary of the calibrated weights assigned to each history matching (HM) term in the global objective function (OF) for the synthetic reservoir (SRM-6, Egg model) and Siberian reference (SR) field model.

Model (Term)	WOPR	WWPR	WGPR	WWIR	WBHP	WBP9
SRM-6	1	1	–	1	0.430 for Production Wells 0.340 for Injection Wells	–
Egg	1	0.242	–	0.424	0.200	–
SR field	1	0.879	0.961	0.722	0.102	0.090

Note: WOPR—well oil production rate; WWPR—well water production rate; WGPR—well gas production rate; WWIR—well water injection rate; WBHP—well bottom-hole pressure; WBP9—wellbore pressure in the 3 × 3 cell block centered on the well. In the cases of SRM-6 and Egg, the models do not include WGPR or WBP9.

2.2.2. Conventional AHM Workflow

The conventional WF began with the construction of a base RSM and the definition of prior uncertainty ranges and distributions for AHM parameters. Sensitivity analysis, conducted using a Tornado chart, informed the experimental design of model realizations. This Tornado sensitivity analysis involves systematically varying each input parameter individually between its lower and upper bounds while keeping all other parameters at their base values, and then measuring the resulting change in the OF [43]. For each parameter, two simulation runs are conducted: one with the parameter set to its minimum value and the other with it set to its maximum. The resulting variation in the OF is then recorded. Consequently, there are a total of 2N + 1 simulations, where N represents the number of AHM parameters. For instance, in the SR field case, there were 511 simulations conducted for 255 parameters, requiring approximately 10 days of computational time at 30 min per run. The parameters are then ranked and displayed in a horizontal bar chart (tornado diagram) sorted by decreasing sensitivity, with the length of each bar indicating the range of impact on the OF. This enables rapid identification of the most influential uncertain parameters for subsequent calibration efforts, and it is widely applied in reservoir uncertainty quantification for reserve estimation and in reducing uncertainty in mature oilfield models [44]. This preparatory stage aimed to exclude from optimization the HM parameters identified as least influential through sensitivity analysis [43]. Key AHM parameters were subsequently selected based on the Tornado analysis and optimized using the PSO algorithm, resulting in the first ensemble of history-matched models. The quality of these models and the optimization outcomes were later compared to those achieved with the SHAP-assisted WF.

2.2.3. CatBoost Model

CatBoost is an ML algorithm developed in 2017 [45], specializing in handling categorical features within a gradient-boosting framework, ensuring high computational efficiency and prediction accuracy [46]. The CatBoost algorithm's unique approach includes two key innovations: Oblivious Trees (symmetric decision trees) and Ordered Boosting, which work together to minimize overfitting, reduce gradient bias, and prevent prediction shifts, resulting in better generalization. In the current study, all calculations and data analyses were performed using Python 3.11.5 in the Jupyter Notebook (ver.7) environment, which was run via the Visual Studio Code IDE (v1.91.0). The workflow relied on the following libraries: scikit-learn (v0.24.0) for preprocessing and evaluation, pandas (v1.3.0) and numpy (v1.20.0) for data manipulation and numerical operations, matplotlib ($\geq$v3.3.0) for visualization, CatBoost (v1.0.0) for surrogate modeling, and SHAP (v0.42.0) for interpretability. This stack ensured full reproducibility, version control, and transparent auditability of the modeling pipeline. The SHAP-assisted WF was implemented using the same base reservoir model and parameter ranges as in the conventional approach. For sensitivity analysis, LHS is preferred over the Monte Carlo method due to its more uniform and efficient coverage of the parameter space with fewer simulations. This reduces the influence of randomness and enhances the reliability of sensitivity results, especially in problems with numerous parameters [47,48]. After evaluating OF values for all LHS models, an ML model (CatBoost Regressor) was trained to replicate the relationship between AHM input parameters and the OF, which served as the output vector. In general, the algorithm evaluates all possible splits for numerical features. While CatBoost is widely recognized for its native handling of categorical features (e.g., lithofacies or region multipliers) [28,46,49], its primary advantage in this study—where only continuous parameters were utilized—lies in its use of oblivious decision trees (symmetric trees) [28,46,49]. This architectural feature strictly limits the tree depth and balances the splits, making the algorithm exceptionally robust against overfit-

ting, which is critical when training on relatively small Latin Hypercube Sampling (LHS) datasets typical in reservoir simulation [28,46,49]. To ensure optimal model performance and reliable SHAP value extraction, the CatBoost regressor underwent systematic hyperparameter tuning using a Grid Search methodology. The dataset was split into an 80/20 train–test ratio. The hyperparameter search space included: number of iterations [30, 50, 100, 150, 1000], tree depth [2, 3, 5, 7, 9], learning rate [0.01, 0.05, 0.07, 0.1], and L_2 regularization term (l2_leaf_reg) [1, 3, 5, 7, 9]. The robustness of the model was validated using 5-fold cross-validation. Performance metrics, including the Coefficient of Determination (R^2), Root Mean Squared Error (RMSE), and Mean Absolute Error (MAE), were evaluated. The optimized surrogate models consistently demonstrated satisfactory explanatory power (with R^2 generally exceeding 0.85 on validation folds), confirming their capability to accurately capture the response surface of the objective function. It is important to emphasize that the ML model in this framework is not deployed as a standalone predictive proxy for dynamic forecasting; rather, its sole purpose is to provide a mathematically rigorous surface from which SHAP can extract reliable marginal parameter contributions prior to optimization. Yet, its black-box nature poses challenges for interpretability, especially in sensitive applications. To address this, SHAP provides a principled way to quantify the contribution of each feature to a given prediction, offering both transparency and trust in CatBoost's decisions [50]. The next subsection describes the SHAP value methodology.

2.2.4. SHAP-Based Feature Interpretation

The Shapley value, proposed by Lloyd Shapley in 1953, originates from coalitional game theory [51]. SHAP is a model interpretation technique introduced to address ML's "black-box" problem [33]. The additive feature attribution method elucidates model predictions by decomposing outputs into the aggregate of individual feature contributions. This methodology preserves interpretability and theoretical coherence across diverse model types, including gradient boosting [52]. The process can be mathematically articulated as [52]:

$$f(z^{\bullet}) = \phi_0 + \sum_{i=0}^{M} \phi_i z_i^{\bullet} \tag{2}$$

where f represents the original prediction model, $z^{\bullet}$ simplifies the input features (where each feature is either present or absent, controlled via a binary masking hyperparameter), φ_0 is a baseline when no inputs are present, M stands for the number of simplified input features, and φ_i represents the contribution of the i-th feature to the output, i.e., the Shapley value.

Multiple techniques exist for estimating SHAP values, including Kernel SHAP, Deep SHAP, and Tree SHAP. Each method is tailored for specific machine learning models, highlighting the versatility of SHAP [33,53]. SHAP values are interpreted in relation to input features (in this case, HM parameters) and model outputs (here, OF), rather than the model's architecture. A primary benefit of SHAP is its interpretable outcome. The marginal contribution of each feature to model predictions can be quantified using various statistical measures of the SHAP values. A metric based on RMSE can provide enhanced sensitivity to extreme variations in feature contributions. The importance of features using the RMSE-based approach is calculated as follows:

$$I_j^{RMSE} = \sqrt{\frac{1}{N}\sum_{i=0}^{N} \phi_{ij}} \tag{3}$$

where ϕ_{ij} represents the SHAP value of feature j for observation i, and N denotes the total number of samples in the dataset. Higher values of I_j^{RMSE} indicate that the feature exerts

a more pronounced influence on model predictions. A notable limitation of the SHAP framework is its dependence on the choice of a background (or reference) distribution, relative to which feature contributions are computed. Specifically, SHAP values quantify the marginal contribution of each feature with respect to the expected model output over this background dataset, effectively, the model's bias term under that distribution. If the background data are not representative of the target population or deployment context (e.g., due to dataset shift, class imbalance, or sampling bias), the resulting explanations may be systematically misleading, as they reflect deviations from a potentially biased baseline rather than an objective neutral point. Determining whether the entire dataset, or the chosen background subset, is itself shifted requires careful validation, such as distributional comparison between training, validation, and test sets using statistical tests (e.g., Kolmogorov–Smirnov, MMD) or domain knowledge. Beyond this, SHAP exhibits several less obvious constraints: (1) computational intractability for exact Shapley value estimation in complex models, often necessitating approximations that may introduce their own biases [54,55]; (2) the implicit assumption of feature independence during the marginalization process, which can yield counterintuitive attributions when features are strongly correlated; and (3) the fact that SHAP values explain deviations from the mean prediction rather than absolute model outputs, which may obscure the interpretability of individual predictions in contexts where the baseline itself is poorly calibrated or uninformative. In the current study, the SHAP values were then calculated to quantify each parameter's contribution to the OF. Based on SHAP analysis, parameters were ranked by importance similarly to the Tornado sensitivity experiment. However, unlike the Tornado approach, SHAP accounts for the simultaneous variation of all parameters, capturing their interdependent effects. Moreover, SHAP analysis identified optimal value ranges for each HM parameter, intervals where OF tends to decrease, allowing refinement of the initial uncertainty ranges before optimization. The next subsection describes the PSO method and the settings for its selected hyperparameters.

2.2.5. Particle Swarm Optimization (PSO)

PSO, originally proposed by Eberhart and Kennedy in 1995 [56], is a population-based metaheuristic inspired by the collective behavior of social organisms such as bird flocks and fish schools. In PSO, a group of candidate solutions, referred to as particles, explores the search space cooperatively in order to identify an optimal or near-optimal solution. Each particle represents a potential solution and adjusts its movement in the search space by considering both its own best experience and the best solution found by the entire swarm. This information-sharing mechanism enables an effective balance between exploration of new regions and exploitation of promising areas, which contributes to the robustness and simplicity of the algorithm [56,57]. Due to its ease of implementation, low computational cost, and strong global search capability, PSO has been widely adopted in optimization tasks across various engineering and scientific domains [56–59]. In petroleum engineering applications, PSO has proven valuable for optimizing drilling parameters [60], modeling complex reservoir properties [57], and enhancing ML model performance [61,62]. Moreover, PSO is often employed as an optimization component within machine learning and ensemble modeling approaches, where it enhances model performance and convergence behavior [61,62]. In the present study, PSO was implemented with fixed hyperparameters across all iterations and both WFs to ensure methodological consistency; only the random SEED varied stochastically. Specifically, for each run R (R = 1–10), the SEED was randomly selected once, documented, and subsequently reused for the corresponding run in both WFs, resulting in differing SEEDs across runs while maintaining consistency between WFs on a run-by-run basis. This design removes confounding from optimizer

randomness and enables a fair comparison of optimization results in both WFs; all SEEDs and hyperparameters were logged to ensure reproducibility. The PSO algorithm was implemented with the following hyperparameters: swarm size = 30, initial inertia = 0.742401, final inertia = 0.627836, nostalgia = 0.74137, sociality = 1.054664, damping factor = 1, and "seed" = "variable". In the final step, two alternative strategies for running the PSO algorithm were considered. The first used the conventional approach, excluding the least influential parameters identified by Tornado analysis from optimization (see Figure 2). The second relied exclusively on SHAP to determine the updated parameter set and ranges. Both WFs were compared under identical conditions, applying the same OF configuration and optimization settings. For cases excluding non-significant parameters from the HM process, their fixed base values remained consistent across experiments. Following the development of the synthetic models (SRM-6 and Egg models) and the SR field methodology framework, the next section explains the obtained results and discusses the development of the SHAP-assisted WF in comparison with the conventional WF.

3. Results and Discussion

This section presents the results of a systematic evaluation of the proposed SHAP-assisted HM-WF across three distinct reservoir models: the synthetic SRM-6 model (see Section 3.1), the benchmark Egg model (see Section 3.2), and the real-world SR field (see Section 3.3). The analysis focuses on parameter sensitivity, range reduction, convergence behavior, and production match quality results, comparing the conventional HM-WFs with those augmented by SHAP-driven feature interpretation and constraint refinement.

3.1. SRM–6 Synthetic Model

3.1.1. SHAP Dependence Range Reduction Plots Across SRM–6 Model

The global sensitivity of HM parameters in the SRM-6 model was evaluated using SHAP beeswarm plots and Tornado diagrams, revealing divergent yet complementary insights into parameter influence on the OF [63,64]. Figure 5a (Tornado plot) quantifies OF variation (%), while Figure 5b (SHAP beeswarm) maps feature importance via game-theoretic marginal contributions, capturing non-linear and interaction effects.

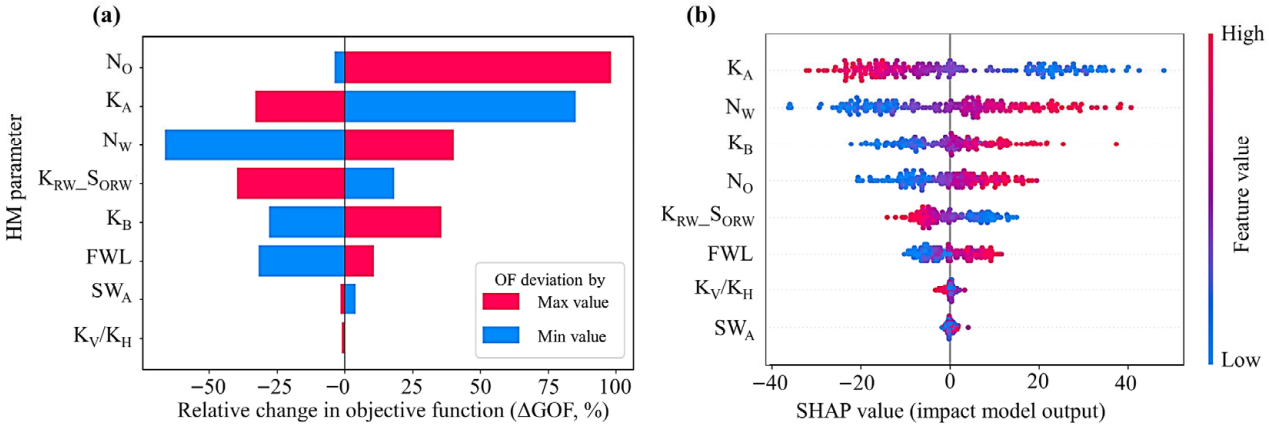


Figure 5. Global sensitivity analysis of history matching (HM) parameters in the synthetic reservoir model (SRM-6): (**a**) Tornado plot quantifying the relative change in global objective function (ΔGOF, %); (**b**) SHAP beeswarm plot illustrating feature importance via game-theoretic marginal contributions, with color intensity indicating high (red) to low (blue) feature value. K_A, K_B—porosity–permeability coefficients; N_w, N_o—Corey exponents for water and oil relative permeability; $K_{rw_S_{orw}}$—water relative permeability at residual oil saturation; FWL—free water level depth (m); K_v/K_h—vertical permeability anisotropy coefficient; SW_A—first coefficient in the natural logarithmic J-function for water saturation.

The selected sensitivity analyses indicate that the parameters "K_v/K_h" and "SW_A" have minimal influence on the change in the OF. Vertical permeability anisotropy has a negligible impact in vertical wells due to minimal vertical flow gradients, while SW_A primarily affects early-time saturation profiles, consistent with its role in the J-function's natural logarithmic form [63,64]. Consequently, these parameters can be fixed at their base values. Notably, the parameter importance ranking obtained via SHAP differs from that of the Tornado analysis, providing a revised perspective on the RSM's response to changes in HM parameters.

Significantly, SHAP dependence plots enable the determination of credible value ranges for HM parameters, as illustrated in Figure 6. Intervals along the *X*-axis (HM parameter value) where the SHAP value on the *Y*-axis consistently remains negative correspond to regions where the OF tends to decrease relative to the value of the SHAP algorithm's base model. For parameters such as "K_A" and "N_w," stable trends indicate clearly defined range constraints. In contrast, "SW_A" exhibits scattered and non-monotonic behavior, reflecting weak sensitivity, consistent with its negligible impact identified in Figure 5. Restricting the optimization algorithm to these parameters facilitates the efficient identification of a set of history-matched models. The SHAP analysis was based solely on the 200-model LHS dataset.

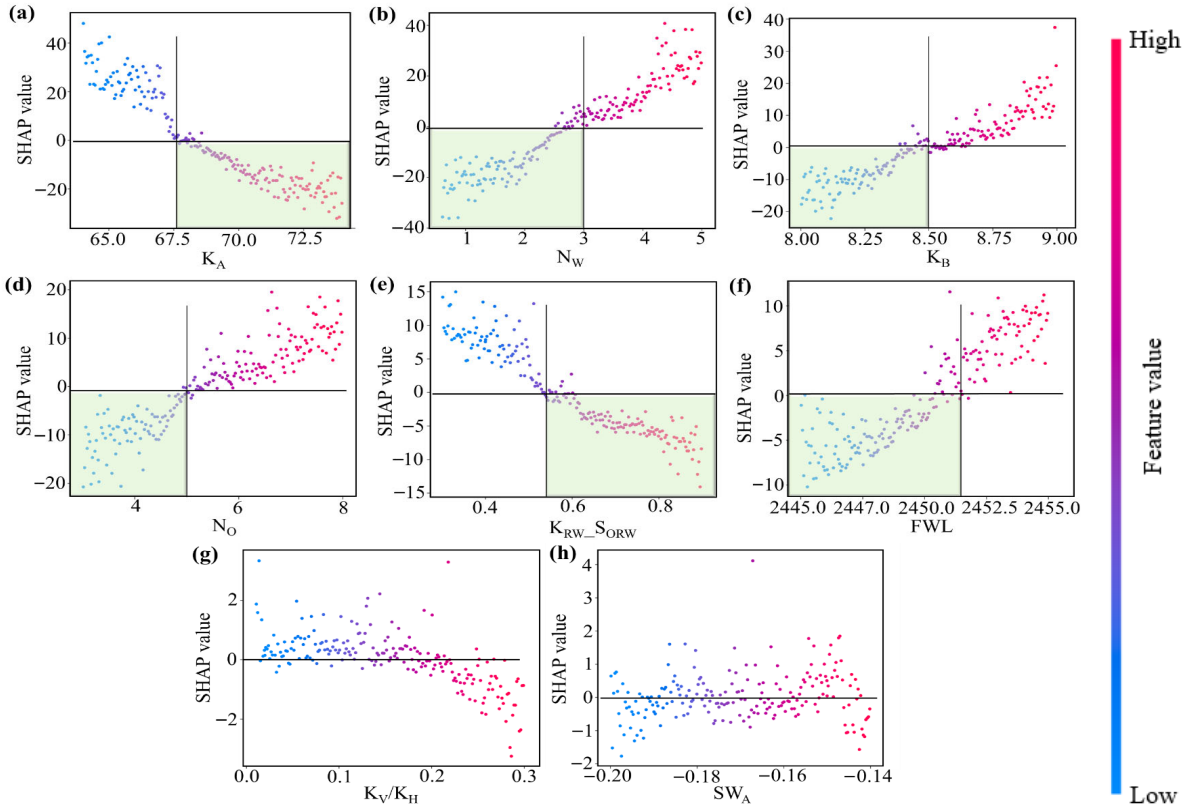


Figure 6. Synthetic reservoir model (SRM-6) SHAP dependence plots: Cross-plots of the SHAP values against the HM parameter values: (**a**) K_A—the first coefficient in the exponential porosity–permeability equation; (**b**) N_w—the Corey exponent of relative permeability for water; (**c**) K_B—the second coefficient in the exponential porosity–permeability equation; (**d**) N_o—the Corey exponent of relative permeability for oil; (**e**) $K_{rw}_S_{orw}$—water relative permeability at residual oil saturation; (**f**) FWL—free water level depth (m); (**g**) K_v/K_h—vertical permeability anisotropy coefficient; (**h**) SW_A—the first coefficient in the natural logarithmic water saturation-J-function equation. The green area indicates the range of values for each HM parameter, facilitating the subsequent initialization of PSO in a SHAP-assisted workflow.

Occasionally, for parameters exhibiting non-monotonic or scattered SHAP dependence (e.g., SW_A in Figure 6h), range redefinition is not justified due to insufficient signal strength. To eliminate this phenomenon, the initial sample can be supplemented with new RSMs to provide the algorithm with more data [65]. Moreover, the hyperparameters of the ML algorithm can be reset if there are concerns about the model's performance, or alternative ML algorithms can be explored. The adjusted range of HM parameters, based on the analysis of SHAP dependence plots, is detailed in Table 5. The "Range reduction" column represents the percentage decrease in ranges for the SHAP-assisted WF relative to the conventional WF.

Table 5. Synthetic reservoir model (SRM-6) parameter ranges in conventional and SHAP-assisted workflows, with the percentage reduction of initial ranges in SHAP-assisted WF relative to the conventional approach.

HM Parameters	Conventional WF (Initial Ranges)		SHAP-Assisted WF (Redefined Ranges)		Range Reduction
	Min. Value	Max. Value	Min. Value	Max. Value	%
FWL	2445	2455	2445	2451	40.0
N_o	3	8	3	5	60.0
N_w	0.6	5.0	0.6	3.0	45.5
$K_{rw}_S_{orw}$	0.30	0.90	0.55	0.90	41.7
K_A	64	74	68	74	40.0
K_B	8.0	9.0	8.0	8.5	50.0

Note: FWL—Free water level depth, m; N_o—Corey exponent of relative permeability for oil; N_w—Corey exponent of relative permeability for water; $K_{rw}_S_{orw}$—Water relative permeability at residual oil saturation; K_A—1st coefficient in the exponential porosity–permeability equation; K_B—2nd coefficient in the exponential porosity–permeability equation. Fixed at the base value: K_v/K_h—Vertical permeability anisotropy coefficient; SW_A—1st coefficient in the natural logarithmic water saturation-J-function equation.

3.1.2. Production Match Quality Across SRM–6 Model

To evaluate the impact of SHAP-guided parameter constraints on optimization efficiency, the convergence behavior of the GOF was compared between conventional and SHAP-assisted WFs across 17 PSO generations. Figure 7 shows that the SHAP-assisted WF consistently achieves lower median GOF values and reduced interquartile spread from early generations onward. The comparative box-plot analysis demonstrates that both conventional and SHAP-assisted WFs efficiently reduce both median and minimum GOF values over successive generations. In the early cycles, the SHAP-assisted approach consistently achieves much lower medians (for example, 12.8 versus 42.3 at 1st Generation) and lower minimum GOF values (2.21 versus 2.76 at 1st Generation) than the conventional workflow. SHAP-assisted ensembles maintain a 30–70% advantage in median and average GOF over conventional ensembles throughout the optimization, while the minimum GOF reached by SHAP-assisted models reaches a value below 1 as early as the 8th Generation, a threshold not achieved by the conventional approach in the first 10 generations. This improvement arises because the SHAP-assisted WF increases optimization efficiency by directing the search algorithm toward more meaningful areas of the parameter space, thereby minimizing exploration of irrelevant or redundant solutions [66].

Additionally, Figure 8 depicts a comparable trend in the oil production rate curves, contrasting the conventional and SHAP-assisted WFs throughout PSO generations, wherein the optimization algorithm operates within a more concentrated region and infrequently investigates unproductive areas of the solution space. At the 1st generation (Figure 8a,d), both WFs exhibit broad uncertainty bands; however, the SHAP-assisted ensemble already shows tighter bounds and better initial alignment with history. By the 9th generation (Figure 8b,e), the SHAP-assisted WF demonstrates significantly reduced spread and improved match fidelity throughout the production period. At convergence (17th generation,

Figure 8c,f), the SHAP-assisted ensemble remains tightly clustered around historical data, while the conventional ensemble still exhibits residual outliers.

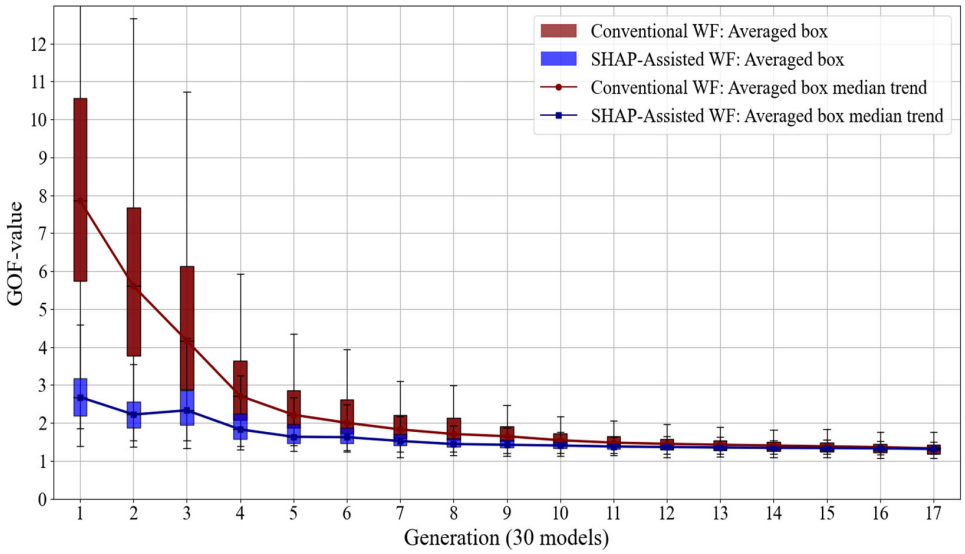


Figure 7. Comparison of global objective function (GOF) convergence behavior in the synthetic reservoir model (SRM-6) between the conventional WF and the SHAP-assisted WF. Boxplots represent the averaged GOF distribution across 10 PSO initializations for each WF, aggregated over 17 generations. Brown and blue boxplots correspond to the conventional and SHAP-assisted WFs, respectively. Black circles indicate the generation numbers corresponding to the production schedules shown below.

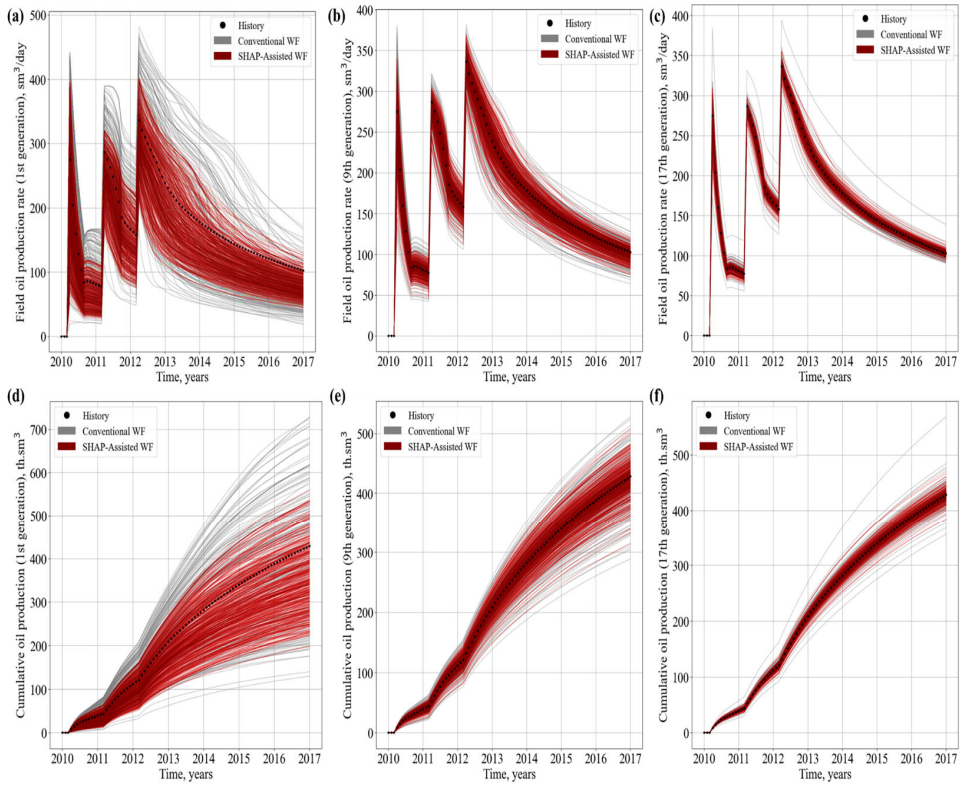


Figure 8. Synthetic reservoir model (SRM-6) oil production comparison between conventional and SHAP-assisted workflows (WFs): (**a**) Field oil production rate at the 1st generation; (**b**) Field oil production rate at the 9th generation; (**c**) Field oil production rate at the 17th generation; (**d**) Cumulative oil production at the 1st generation; (**e**) Cumulative oil production at the 9th generation; and (**f**) Cumulative oil production at the 17th generation.

3.2. Egg Model Benchmark

3.2.1. SHAP Dependence Range Reduction Plots Across Egg Model

Unlike the SRM-6 results, the sensitivity analysis for the Egg model, as illustrated in Figure 9, revealed only minor variations in the evaluation of less influential parameters and in the ranking of other key HM parameters. This limited contrast is primarily attributed to the artificial nature of the Egg model, which represents a low-depletion system producing fluids under relatively small drawdowns. Under these conditions, the wells have sufficient productivity to deliver the target fluid volumes and ensure a consistent adjustment of bottomhole pressures.

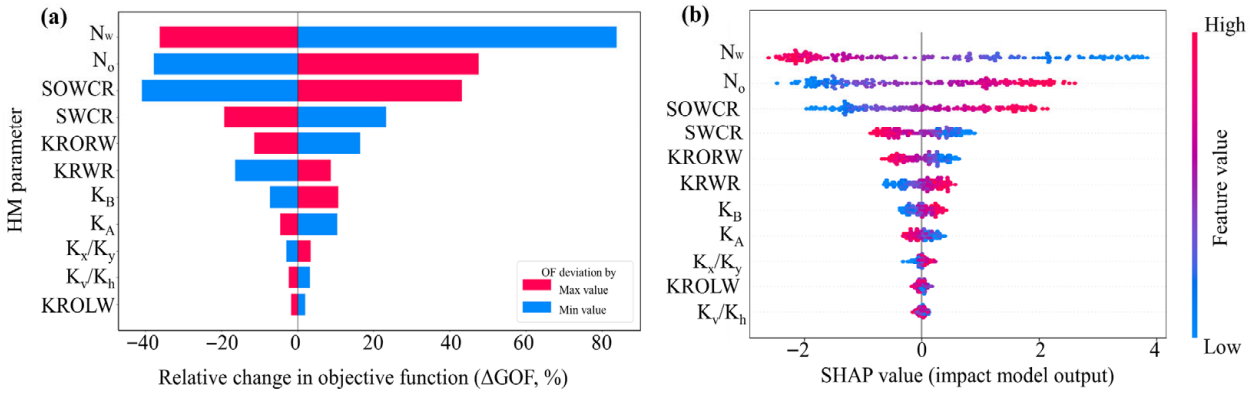


Figure 9. Sensitivity analysis of the Egg model, identifying the key history matching (HM) parameters using: (**a**) Tornado plot quantifying the relative change in global objective function (ΔGOF, %); (**b**) SHAP beeswarm plot illustrating feature importance via game-theoretic marginal contributions, with color intensity indicating high (red) to low (blue) feature value. K_A—1st coefficient in the exponential porosity–permeability equation; K_B—2nd coefficient in the exponential porosity–permeability equation; K_x/K_y—Permeability anisotropy coefficient in XY direction; K_v/K_h—Vertical permeability anisotropy coefficient; SWCR—Critical water saturation; SOWCR—Residual oil saturation; KROLW—The relative phase permeability of oil with residual water saturation; KRORW—The relative phase permeability of oil with critical water saturation; KRWR—The relative phase permeability of water with residual oil saturation; N_o—The degree of Corey for the relative phase curve of oil; N_W—The degree of Corey for the relative phase curve of water.

Consequently, the relative permeability HM parameters emerged as the dominant factors in reproducing the oil and water production profiles. Their sensitivity is primarily governed by the critical saturations, which delineate the mobile flow region, and by the Corey exponents, which determine the curvature of the relative permeability functions. The analysis also identified three HM parameters with negligible impact. Consistent with the preceding SRM-6 model, permeability anisotropy in all directions exerts minimal influence on the production performance of vertical wells. Similarly, the relative permeability of oil under immobile water conditions shows limited effect, as the wells are located entirely within a pure oil zone and maintain sufficient productivity for accurate matching of oil rates. These parameters were fixed at their base values prior to the PSO initialization. SHAP dependence plots were employed to determine plausible value ranges for HM parameters, as shown in Figure 10.

The SHAP dependence plots identify the ranges of HM parameter values where the OF tends to decrease relative to the base model. These specific intervals were redefined in the SHAP-assisted WF. Table 6 presents the original and redefined ranges for both conventional and SHAP-assisted WFs, along with the percentage reduction of initial ranges observed in the SHAP-assisted WF. These reductions range from 28.6% to 50.0% across key relative permeability and porosity–permeability parameters. Notably, parameters such as SWCR,

SOWCR, and N_o demonstrated the highest range compression, reflecting their significant influence on production behavior and confirming SHAP's capability to identify critical areas for targeted optimization.

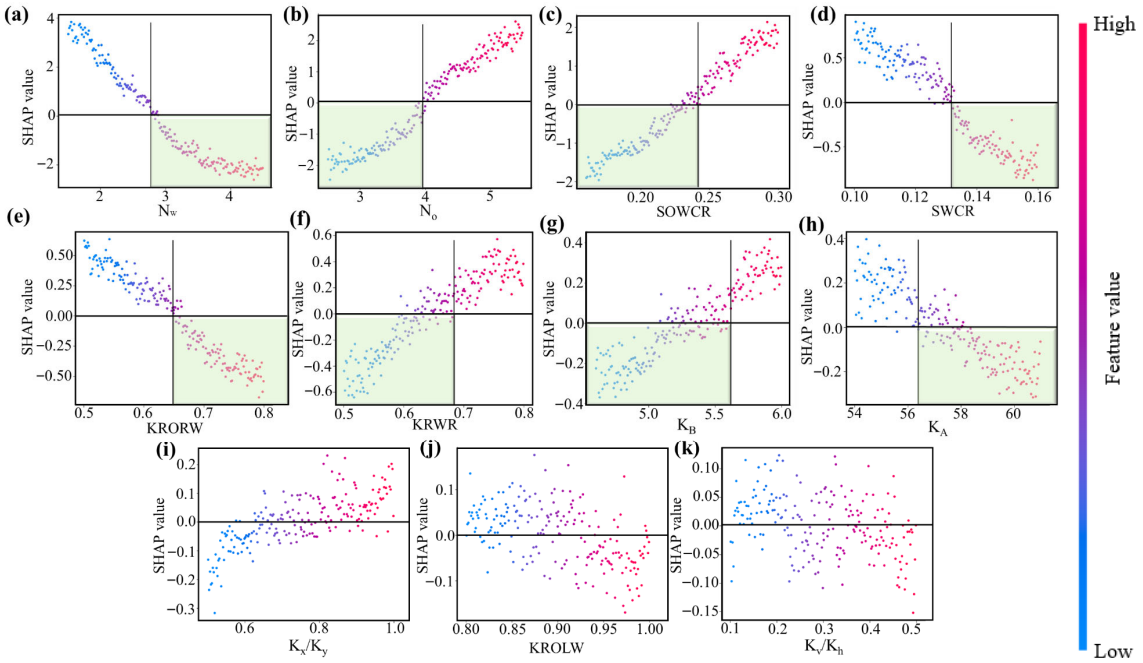


Figure 10. Egg model SHAP dependence plots: Cross-plots between the SHAP values and the history matching (HM) parameter values: (**a**) NW—The degree of Corey for the relative phase curve of water; (**b**) No—The degree of Corey for the relative phase curve of oil; (**c**) SOWCR—Residual oil saturation; (**d**) SWCR—Critical water saturation; (**e**) KRORW—The relative phase permeability of oil with critical water saturation; (**f**) KRWR—The relative phase permeability of water with residual oil saturation; (**g**) KB—2nd coefficient in the exponential porosity–permeability equation; (**h**) KA—1st coefficient in the exponential porosity–permeability equation; (**i**) Kx/Ky—Permeability anisotropy coefficient in XY direction; (**j**) KROLW—The relative phase permeability of oil with residual water saturation; (**k**) Kv/Kh—Vertical permeability anisotropy coefficient. The green area shows the range of values for each HM parameter for subsequent initialization of PSO in a SHAP-assisted workflow.

Table 6. Egg model parameter ranges in conventional and SHAP-assisted workflows (WFs) with the percentage reduction of initial ranges in SHAP-assisted WF relative to the conventional approach.

HM Parameters	Conventional WF (Initial Ranges)		SHAP-Assisted WF (Redefined Ranges)		Range Reduction
	Min. Value	Max. Value	Min. Value	Max. Value	%
K_A	54.0	61.0	56.5	61.0	35.8
K_B	4.6	6.0	4.6	5.6	28.6
SWCR	0.10	0.16	0.13	0.16	50.0
SOWCR	0.16	0.30	0.16	0.24	43.0
KRORW	0.50	0.80	0.65	0.80	50.0
KRWR	0.50	0.80	0.50	0.68	40.0
N_o	2.5	5.5	2.5	4.0	50.0
N_W	1.5	4.5	2.9	4.5	46.7

Note: K_A—1st coefficient in the exponential porosity–permeability equation; K_B—2nd coefficient in the exponential porosity–permeability equation; SWCR—Critical water saturation; SOWCR—Residual oil saturation; KRORW—The relative phase permeability of oil with critical water saturation; KRWR—The relative phase permeability of water with residual oil saturation; N_o—The degree of Corey for the relative phase curve of oil; NW—The degree of Corey for the relative phase curve of water. Fixed at the base value: K_x/K_y—Permeability anisotropy coefficient in XY direction; KROLW—The relative phase permeability of oil with residual water saturation; K_v/K_h—Vertical permeability anisotropy coefficient.

3.2.2. Production Match Quality Across Egg Model

The comparison of the behavior of the GOF in the conventional WF and the SHAP-assisted WF over generations is shown in Figure 11. The superior early performance of the SHAP-assisted WF (19–66% lower median GOF from the 1st to the 6th generation) is primarily due to SHAP-guided parameter screening and range refinement, which restrict the optimizer to regions of the parameter space empirically associated with lower misfit values. As a result, PSO spends fewer iterations exploring non-informative or high-misfit regions, leading to faster convergence. From the 7th to 17th generation, the advantage of the SHAP-assisted WF decreases to 2–16%. This diminishing difference reflects the progressive saturation of the refined search space, where both workflows increasingly explore similar high-quality regions and approach comparable local optima. Accordingly, the minimum GOF achieved by the SHAP-assisted WF is lower in early generations (up to 0.15 difference) but converges toward conventional values in later stages (difference < 0.08). This behavior confirms that SHAP primarily improves optimization efficiency rather than altering the final attainable solution quality, explaining why both workflows converge to statistically similar results as the number of generations increases.

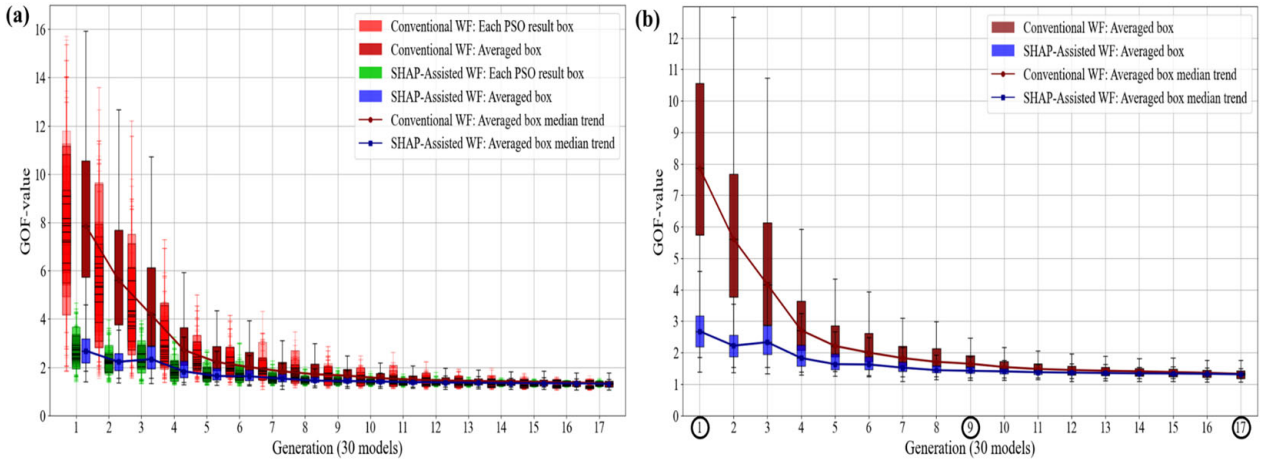


Figure 11. Comparison of global objective function (GOF) behavior in the synthetic reservoir model (Egg model) between the conventional WF and the SHAP-assisted WF: (**a**) The red and green boxplots show the distribution of GOF for each generation, across all PSO initializations and WF types; (**b**) Enlarged averaged boxplots. The brown and blue boxplots represent the average distribution across 10 PSO initializations for each WF, aggregated over generations. Black circles indicate the generation numbers corresponding to the production schedules shown below.

The analysis of the oil production curves in Figure 12 reveals a consistent trend. Similar to the SRM-6 model, the optimization algorithm demonstrates a reduced likelihood of entering irrelevant solution domains when SHAP values are incorporated. At the 1st generation (Figure 12a,d), both WFs show broad production uncertainty, but the SHAP-assisted ensemble already exhibits tighter bounds and improved alignment with historical data. By the 9th generation (Figure 12b,e), both WFs demonstrate a similar variance in the production curves, although for a fair assessment, in the SHAP-assisted approach, the production curves are clustered more closely around the historical data, even if this superiority is insignificant. The reason for this improvement in the SHAP-assisted WF is that it narrows the parameter search space early on by focusing the optimizer on the most influential parameters. At convergence (17th generation, Figure 12c,f), the difference between the SHAP-assisted ensemble and the conventional workflow becomes negligible, with both approaches demonstrating similarly tight clustering around the historical data. This is because, by the 17th generation, the search space has been sufficiently explored

and refined, and both methods eventually converge to similar optimal solutions. At this stage, SHAP's early advantage in guiding the optimization becomes less relevant, as both workflows have sufficiently explored the parameter space, resulting in similar final outcomes.

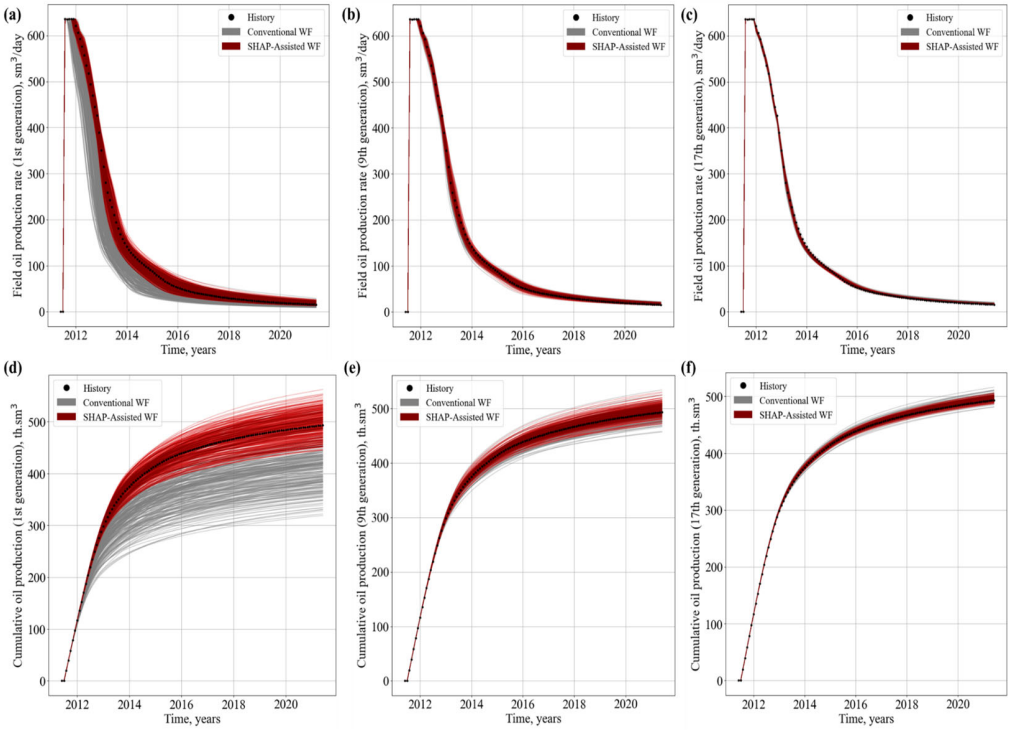


Figure 12. Synthetic reservoir model (Egg model) oil production comparison between conventional and SHAP-assisted workflows: (**a**) Field oil production rate at the 1st generation; (**b**) Field oil production rate at the 9th generation; (**c**) Field oil production rate at the 17th generation; (**d**) Cumulative oil production at the 1st generation; (**e**) Cumulative oil production at the 9th generation; and (**f**) Cumulative oil production at the 17th generation.

A critical consideration when aggressively reducing the parameter search space (by 29–50%) is the risk of inadvertently excluding the "true" global optimum. To evaluate this, the redefined bounds were cross-referenced with the known "True Values" of the synthetic models (Tables 1 and 2). For the SRM-6 model, all true values were successfully retained within the SHAP-refined bounds (Table 5). For the Egg model, the vast majority of true parameters were preserved; however, highly correlated parameters (such as the porosity–permeability coefficient K_A and residual oil saturation *SOWCR*) fell marginally outside the redefined intervals (Table 6). This phenomenon highlights a fundamental characteristic of reservoir history matching: the non-uniqueness of the inverse problem (equifinality). In complex parameter spaces, particularly those governing relative permeabilities, different combinations of variables can compensate for one another to produce an identical dynamic response. The SHAP analysis does not merely hunt for a single deterministic "true" point; rather, it identifies a highly productive sub-space—a manifold of equivalent solutions—where parameter interactions consistently minimize the objective function. As demonstrated by the superior early convergence and matching quality in the Egg model (Figures 11 and 12), the data-driven range reduction focuses the global search capability on the most viable parameter combinations, successfully achieving an optimal equivalent solution without compromising the overall robustness of the algorithm.

3.3. Siberian Reference Field Real-World Application

3.3.1. SHAP Dependence Range Reduction Plots Across Siberian Reference Field

After estimating the uncertainties and parameterizing the HM variables, the field reservoir model is initially calibrated using 255 parameters: from the seismic horizon reference position to the endpoints of the relative permeability. Because the dataset is very large, only the 25 most important HM parameters (10%) were selected for the demonstration of the proposed approach. The purpose of this reduction was not to reflect the full complexity of the field, but to focus on illustrating the application of the method itself. For instance, the parameters "φ_m" (porosity configuration coefficient) and "FWL (4)" (water-oil contact in the 4th block) control storage capacity at two scales—the full hydrodynamic model and the designated unit block—thereby capturing both field-level volumetric effects and local compartmentalization [67,68]. These parameters were selected to illustrate how the methodology works in real-world cases while maintaining a manageable number of parameters for demonstration. In parallel, for example, region-specific KRWR parameters control water mobility in areas with the largest contribution to total water production. However, matching of water rates has been impeded by significant uncertainty in fault geometry and transmissibility and by potential injection-induced hydraulic fractures in injection wells [69,70]. Under these conditions, HM parameters controlling water mobility exert a significant influence on the OF. In real practice, it is possible to evaluate and automatically fine-tune the entire set of HM parameters and their ranges. Similar to the synthetic models (SRM-6 and Egg models), sensitivity analysis was conducted using both Tornado and SHAP beeswarm plots. Since the set of HM parameters is large, the sensitivity estimates varied significantly between the conventional and SHAP-assisted methodologies (Figure 13), illustrating the impact of using different sensitivity analysis methods on the selection of parameters.

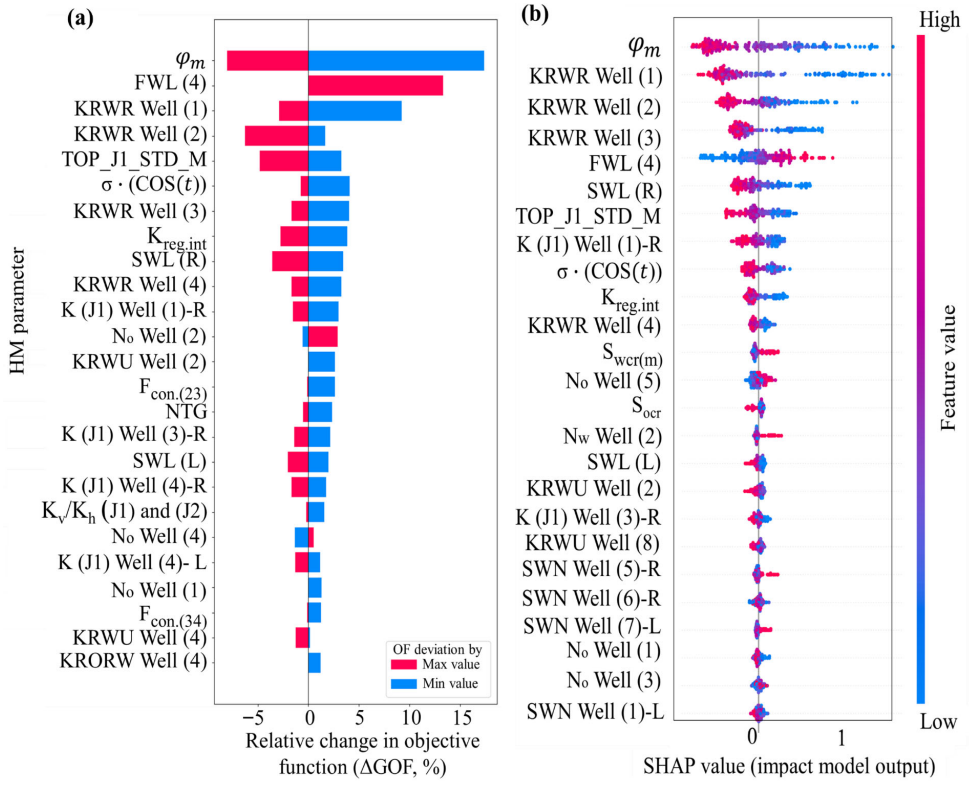


Figure 13. Global sensitivity analysis of history matching (HM) parameters in the Siberian reference (SR) field: (**a**) Tornado plot quantifying the relative change in global objective function (ΔGOF, %); (**b**) SHAP beeswarm plot illustrating feature importance via game-theoretic marginal contributions, with color intensity indicating high (red) to low (blue) feature value.

Sensitivity analysis in the conventional WF reveals that while the top ranks are dominated by local parameters, the primary influence among global parameters is attributed to TOP_J1_STD_M. Although ranked 5th overall in the Tornado analysis, this parameter (which modulates the position of the J1 formation top) contributes notably to the overall GOF variation. The sensitivity analysis tends to lower the formation top and raise the water–oil contact in block 4 (FWL (4)) to increase water production. However, since these are global parameters, they significantly affect the entire model and production across all wells. In contrast, SHAP-based sensitivity analysis identifies a more pronounced impact of water relative permeability parameters in regions of predominant water production (e.g., KRWR Well (1–4)) and water saturation dependence parameters (SWN Well (5–7)), allowing for a more localized and refined adjustment in these areas. These conclusions presume that the parameterization and uncertainty quantification are sufficient to achieve a matched model, considering the complexity and heterogeneity of the RSM. Figure 14 shows the SHAP dependence plots for the HM parameters.

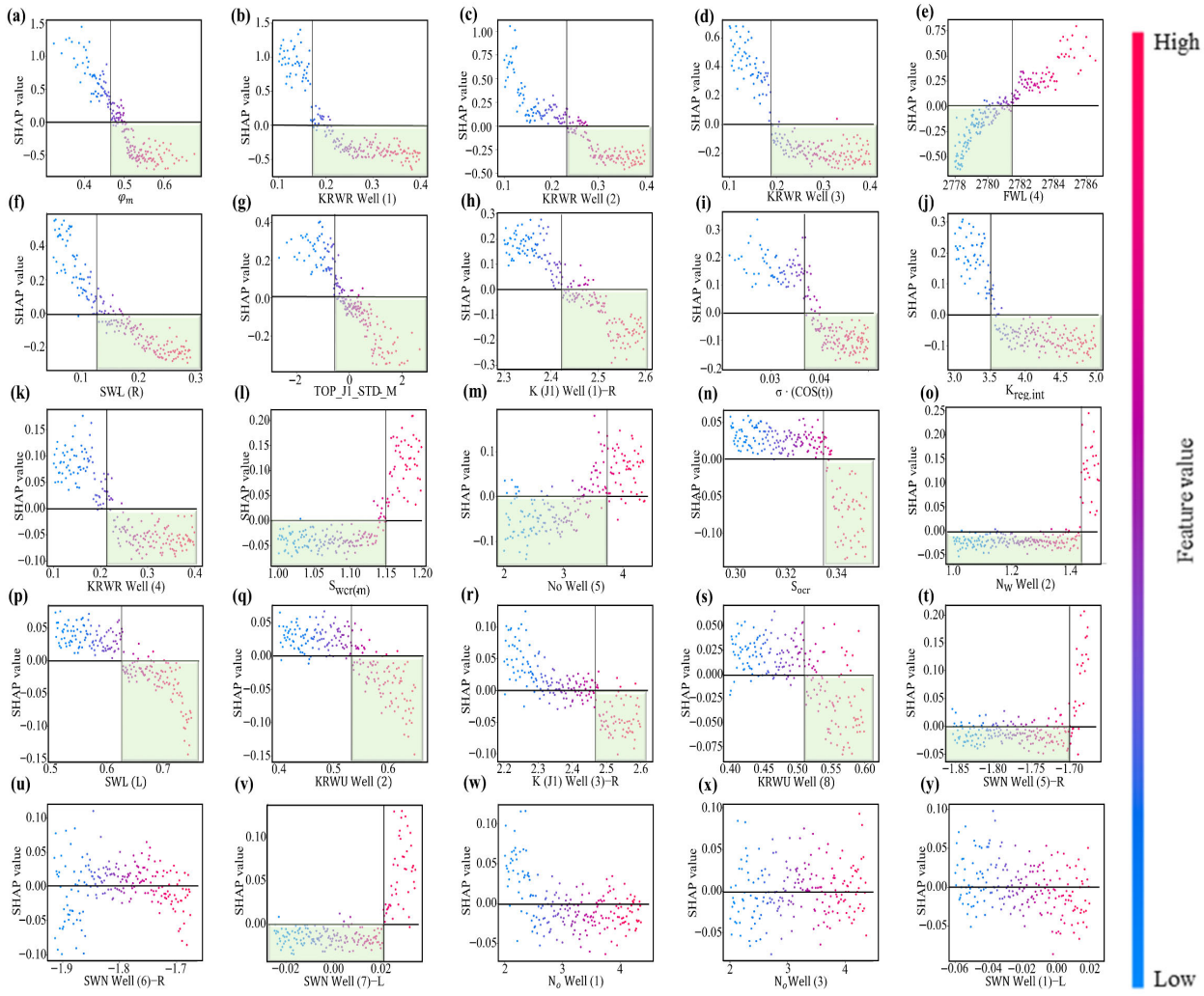


Figure 14. SHAP dependence plots for key history matching (HM) parameters in the Siberian reference (SR) field model: (**a**) φ_m; (**b**) KRWR Well (1); (**c**) KRWR Well (2); (**d**) KRWR Well (3); (**e**) FWL (4); (**f**) SWL (R); (**g**) TOP_J1_STD_M; (**h**) K (J1) Well (1)-R; (**i**) σ · (COS(t)); (**j**) Kreg.int; (**k**) KRWR Well (4); (**l**) $S_{wcr(m)}$; (**m**) No Well (5); (**n**) S_{ocr}; (**o**) N_WWell(2); (**p**) SWL (L); (**q**) KRWUWell(2); (**r**) K (J1) Well (3)-R; (**s**) KRWUWell (8); (**t**) SWNWell (5)-R; (**u**) SWNWell (6)-R; (**v**) SWNWell (7)-L; (**w**) N_oWell (1); (**x**) N_oWell (3); and (**y**) SWNWell (1)-L. The green regions indicate HM parameter ranges where the OF tends to decrease. All abbreviations are listed in the nomenclature.

Consequently, these ranges are selected as redefined boundaries and used to initialize the PSO algorithm. Table 7 presents a systematic comparison of parameter-range transformations across workflow realizations in the SR field model.

Table 7. History matching (HM) parameter ranges across workflow (WF) realizations in the Siberian reference (SR) model: comparison of initial ranges (conventional WF) and redefined ranges (SHAP-assisted WF), with percentage reduction where applicable.

HM Parameter Group	Parameter Designation	Conventional WF (Initial Ranges)		SHAP-Assisted WF (Redefined Ranges)		Range Reduction
		Min. Value	Max. Value	Min. Value	Max. Value	%
Critical oil saturation	S_{ocr}	—	—	0.335	0.352	—
Critical water saturation	$S_{wcr(m)}$	—	—	1.000	1.150	—
Fault conductivity	$F_{con.(23)}$	0	1	—	—	—
	$F_{con.(34)}$	0	1	—	—	—
Fluid contacts	FWL (4)	2778.0	2787.0	2778.0	2781.7	59
Irreducible water saturation	SWL (R)	0.049	0.292	0.130	0.292	33
	SWL (L)	0.508	0.751	0.625	0.751	48
Relative permeability parameters	KRWR Well (1)	0.10	0.40	0.18	0.40	27
	KRWR Well (2)	0.10	0.40	0.23	0.40	43
	KRWR Well (3)	0.10	0.40	0.18	0.40	27
	KRWR Well (4)	0.10	0.40	0.22	0.40	40
	KRWU Well (2)	0.40	0.65	0.53	0.65	52
	KRWU Well (4)	0.40	0.60	—	—	—
	KRWU Well (8)	—	—	0.51	0.60	—
	KRORW Well (4)	0.10	0.40	—	—	—
	N_o Well (1)	2.00	4.37	2.00	4.37	0
	N_o Well (2)	2.00	4.37	—	—	—
	N_o Well (3)	—	—	2.00	4.37	—
	N_o Well (4)	2.00	4.37	—	—	—
	N_o Well (5)	—	—	2.00	3.75	—
	N_w Well (2)	—	—	1.00	1.44	—
Reservoir distribution	NTG	0.39	0.61	—	—	—
	$K_{reg.int}$	3.00	5.00	3.50	5.00	25
	K_v/K_h (J1) and (J2)	0.20	1.00	—	—	—
Reservoir permeability	K (J1) Well (1)-R	2.30	2.60	2.42	2.60	40
	K (J1) Well (3)-R	2.20	2.60	2.47	2.60	68
	K (J1) Well (4)-R	2.20	2.50	—	—	—
	K (J1) Well (4)-L	0.50	1.10	—	—	—
Reservoir porosity	φ_m	0.30	0.70	0.47	0.70	43
Structural surfaces	TOP_J1_STD_M	−3.00	3.00	−0.50	3.00	42
	$\sigma \cdot (COS(t))$	0.020	0.050	0.037	0.050	57
Water saturation in the transition zone	SWN Well (1)-L	—	—	−0.060	−0.020	—
	SWN Well (5)-R	—	—	−1.855	−1.700	—
	SWN Well (6)-R	—	—	−1.915	−1.675	—
	SWN Well (7)-L	—	—	−0.025	0.021	—

Note: All abbreviations can be seen in the nomenclature.

3.3.2. Production Match Quality Across Siberian Reference Field

To assess the scalability of the SHAP-assisted WF under real-field complexity, the convergence behavior of the GOF and the production performance of each fluid type were compared between the conventional and SHAP-guided WFs in the SR field model, as illustrated in Figure 15, which shows box-plots representing the distribution of GOF for each of the 10 PSO realizations (red for conventional WF, green for SHAP-assisted WF). Additionally, for ease of interpretation, an averaged box-plot is presented for each generation from 30 RSM models (brown for conventional WF; blue for SHAP-assisted WF).

The SHAP-assisted WF yields median GOF values that are 7–15% lower than those of the conventional WF, while mean GOF values display a similar quantitative advantage. The minimum GOF achieved by SHAP-assisted ensembles is also lower in every generation,

with margins ranging from 0.2 to over 1.6 in absolute value. Furthermore, the analysis of oil, water and gas production curves corroborates these results as illustrated in Figure 16. The analysis of production curves demonstrates a substantial reduction in production rate mismatches over nearly the entire HM period.

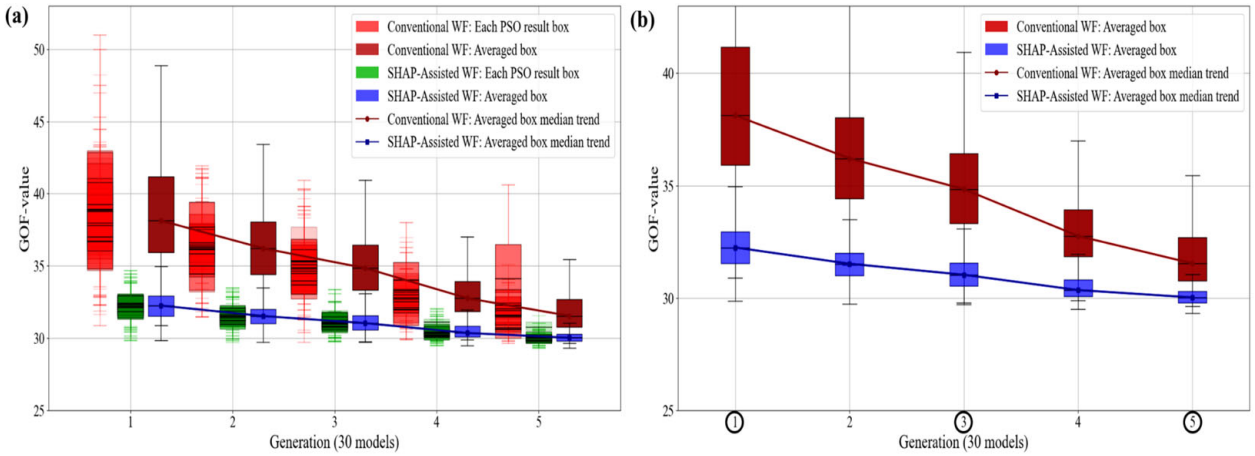


Figure 15. Comparison of global objective function (GOF) behavior in the Siberian reference (SR) field model between the conventional workflow (WF) and the SHAP-assisted WF: (**a**) The red and green boxplots show the distribution of GOF for each generation, across all PSO initializations and WF types; (**b**) Enlarged averaged boxplots. The brown and blue boxplots represent the average distribution across 10 PSO initializations for each WF, aggregated over generations. Black circles indicate the generation numbers corresponding to the production schedules shown below.

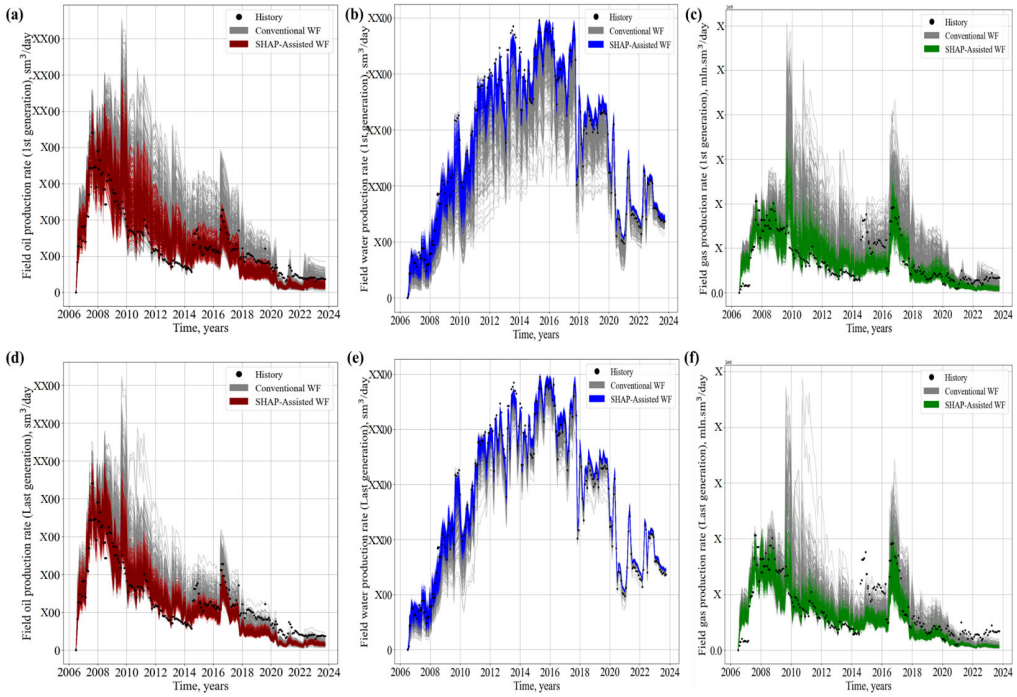


Figure 16. Siberian reference (SR) field optimization behavior comparison between conventional and SHAP-assisted workflows: Field production rate at the 1st generation for (**a**) oil, (**b**) water, and (**c**) gas; Field production rate at the 5th generation for (**d**) oil, (**e**) water, and (**f**) gas. Conventional WF ensembles are shown in gray; SHAP-assisted WF ensembles are shown in red (oil), blue (water), and green (gas). Historical data are indicated by black markers. The actual information regarding the figure has been anonymized because of the data confidentiality constraints set by the partner company.

Overall, the analysis of optimization trajectories across early, intermediate, and late stages (Table 8) demonstrates that SHAP-assisted WF achieves accelerated convergence to equivalent solution quality with substantially greater computational efficiency than conventional approaches. During early optimization (1st generation), SHAP ensembles demonstrate pronounced superiority with median error reductions of 69.8% (SRM-6), 65.9% (Egg), and 15.4% (SR field). This advantage persists through intermediate stages but progressively diminishes. By late optimization (13th–17th generations), relative reductions narrow to 13.4–26.9% (SRM-6), 1.1–5.0% (Egg), and 4.8–7.4% (SR field), converging toward statistically equivalent final GOF values: SRM-6 1.53 vs. 1.33; Egg 1.33 vs. 1.32. Computational savings across all models are quantified in Table 8. SRM-6 and Egg Model each require 1 fewer generation (5.9% reduction), while the SR real field model requires 3 fewer generations (60% reduction in computational cycles), demonstrating that SHAP-assisted optimization achieves equivalent calibration quality with systematically reduced computational burden. While SHAP-assisted optimization does not guarantee superior final model quality, it delivers substantially greater computational efficiency, and practitioners can reduce computational burden by 6–60% while obtaining calibration quality statistically indistinguishable from conventional workflows. The experimental results revealed a critical distinction between SHAP-based and Tornado-based parameter assessment. It was observed that SHAP consistently identified combinations of parameters that yielded systematically high misfit values, which were overlooked by the Tornado method. For example, SHAP analysis revealed subspaces where joint parameter variations consistently produced responses with large objective function values. These areas were excluded before HM, reducing the search space for optimization by a measurable margin (e.g., the 25–68% reduction in parameter uncertainty bounds detailed in Tables 5–7). Critically, Tornado's univariate approach failed to flag these areas because individual parameter perturbations remained within the marginal parameter thresholds. Consequently, the workflows initialized with parameters assessed by SHAP required fewer iterations to reach equivalent calibration thresholds. For instance, in the SRM-6 model (Figure 7), the SHAP-assisted workflow achieved, at generation 2, a median GOF comparable to the conventional workflow at generation 6, effectively yielding an equivalent history match quality while saving 4 optimization generations (i.e., 120 simulator runs per trial). This outcome stems directly from the ability of SHAP to evaluate interactions across a sampled parameter space, a capability absent from sequential, single-parameter analyses. The results demonstrate that SHAP-based pre-assessment enhances HM efficiency by empirically eliminating non-viable regions detectable only through joint evaluation of parameters. This accelerated convergence and improved stability are statistically supported by the narrower interquartile ranges in the convergence distributions (Figures 7, 11 and 15) and the systematically lower standard deviations across all repeated trials (Table 8).

Table 8. Comparison of optimization performance across all RSMs and key optimization stages.

Model	Gen	Median Conv	Median SHAP	Min Conv	Min SHAP	STD Conv	STD SHAP	Median Reduction (%)	Min Reduction (%)
SRM-6	1	42.33	12.79	2.76	2.21	35.23	6.51	69.8	19.9
SRM-6	5	9.35	5.77	2.06	1.67	7.86	3.48	38.2	18.9
SRM-6	9	4.61	3.26	1.08	1.18	3.33	2.37	29.3	−9.2
SRM-6	13	2.59	1.89	0.85	0.92	2.41	1.58	26.9	−8.1
SRM-6	17	1.53	1.33	0.85	0.89	1.52	0.98	13.4	−5.3
Egg	1	7.86	2.68	1.85	1.4	3.21	0.72	65.9	24.4

Table 8. *Cont.*

Model	Gen	Median Conv	Median SHAP	Min Conv	Min SHAP	STD Conv	STD SHAP	Median Reduction (%)	Min Reduction (%)
Egg	5	2.22	1.64	1.4	1.27	0.95	0.46	26.2	9.8
Egg	9	1.65	1.43	1.13	1.21	0.45	0.26	13.7	−7
Egg	13	1.43	1.35	1.12	1.18	0.27	0.13	5	−5.9
Egg	17	1.33	1.32	1.07	1.19	0.16	0.07	1.1	−11
SR field	1	38.13	32.24	30.9	29.85	4	1.02	15.4	3.4
SR field	2	36.21	31.52	31.47	29.74	2.85	0.77	13	5.5
SR field	3	34.84	31.03	29.72	29.78	2.6	0.73	10.9	−0.2
SR field	4	32.76	30.35	29.89	29.49	1.78	0.62	7.4	1.3
SR field	5	31.53	30.02	29.63	29.32	1.83	0.46	4.8	1

Note: Gen—generation number, Conv—Conventional WF, SHAP—SHAP-Assisted WF, and STD—Standard deviation.

Overall, in both synthetic benchmarks (SRM-6 and Egg) and the real-field SR case, the SHAP-assisted WF consistently proved its enhancement in optimization efficiency, achieving equivalent or superior history match quality with 6–60% fewer PSO generations while systematically refining parameter ranges by 25–68% through interpretable, data-driven sensitivity analysis.

4. Recommendations for Future Work

To build upon the current adaptive HM-WF, which integrates ML and SHAP-based sensitivity analysis, several promising directions for future research can be identified as follows.

- The solution space exploration relies on a fixed ensemble of models generated during the initial design of experiments, potentially omitting promising regions that emerge only during later optimization stages. Future work should develop adaptive optimization frameworks that dynamically incorporate newly evaluated models during optimization (e.g., at intermediate re-evaluation stages), enabling iterative expansion of the parameter space with concurrent SHAP analysis to guide sampling toward underexplored yet promising regions.
- Interpretability of parameter importance depends on SHAP values from a single ML algorithm, which may yield biased or non-robust sensitivity rankings due to algorithm-specific learning patterns. This limitation can be addressed by performing SHAP analysis across multiple complementary algorithms (e.g., gradient boosting, random forests, support vector regression) and clustering the resulting values to identify consistent parameter importance trends, thereby enhancing both interpretability and adaptability of the sensitivity assessment.
- The optimization algorithm is initialized with a random population, disregarding high-quality models already identified during design of experiments. A more efficient approach would seed the initial population with top-performing models from the experimental design, combined with SHAP-derived estimates of influential parameter ranges. This informed initialization should accelerate convergence for complex reservoirs, though care must be taken to preserve population diversity and avoid premature convergence.
- Finally, the application to the SR field case revealed that aggressive parameter range narrowing during late-time matching produced over-constrained solutions deviating from historical production data. Future implementations should adopt adaptive constraint strategies with judicious range reduction criteria and improved response sur-

face model parametrization to maintain optimizer flexibility in data-scarce reservoirs while preserving history match quality throughout the entire production timeline.

5. Conclusions

This study presents a Shapley Additive Explanations (SHAP)-assisted workflow that integrates CatBoost regression with SHAP value analysis to refine parameter ranges in automated history matching (AHM). The approach aims to improve match quality, accelerate convergence, and reduce computational cost by identifying influential parameters and constraining their uncertainty ranges prior to optimization. Tested on two synthetic models (SRM-6, the Egg model) and a real-field case (the Siberian reference (SR) field), the framework consistently outperformed conventional Tornado-based sensitivity analysis. Key findings include:

1. Integration of SHAP value analysis with CatBoost regressor: SHAP values extracted directly from existing Latin Hypercube Sampling (LHS) ensembles enable interpretable, model-agnostic sensitivity analysis without additional simulation runs, eliminating the need for dedicated Tornado experiments. In high-dimensional settings (e.g., SR field with 255 HM parameters), Tornado analysis proves impractical, requiring 511 supplementary simulations (approximately 10 days at 30 min per run) with limited analytical utility beyond basic sensitivity ranking. SHAP leverages pre-existing simulation data, providing substantially more efficient feature attribution.
2. Systematic data-driven parameter range refinement: The SHAP-assisted method identified parameter subspaces where the objective function (OF) decreased relative to the base model, allowing targeted range reduction and more efficient PSO initialization. Results demonstrate a 25–68% reduction in parameter uncertainty ranges across the SRM-6, Egg, and SR field models. This data-driven constraint of parameter search spaces directly enables more focused optimization workflows with improved initial conditions.
3. Computationally efficient achievement of equivalent final calibration quality: Comparative analysis of optimization performance across all three reservoir simulation models reveals that the SHAP-assisted workflow achieves equivalent final history match quality while requiring 6–60% fewer optimization cycles. Specifically, SRM-6 and the Egg Model each attain the conventional workflow's final GOF with 1 fewer generation (5.9% reduction), while the SR field model reaches equivalent calibration quality by Generation 2, compared with Generation 5 in the conventional workflow, representing a 60% reduction in required computational cycles. Early-stage optimization demonstrates a pronounced SHAP advantage (69.8% median GOF reduction for SRM-6, 65.9% for Egg, 15.4% for SR field at 1st generation), which progressively diminishes through intermediate stages and converges to statistical equivalence by the final optimization phase. Throughout all optimization stages, SHAP-assisted ensembles consistently exhibit greater stability (lower standard deviation and box-plot range), indicating greater computational efficiency.

Author Contributions: Conceptualization: G.E., A.M.M., I.E.S., M.A.-S. and S.D.; Methodology: G.E., A.M.M. and I.E.S.; Software: A.M.M. and G.E.; Validation: G.E., A.M.M., M.A.-S., G.Y.S., I.E.S., I.V.M. and S.D.; Formal analysis: G.E., A.M.M., I.E.S., M.A.-S. and S.D.; Investigation, G.E., A.M.M., M.A.-S. and I.E.S.; Resources: I.V.M. and I.E.S.; Data curation: A.M.M. and G.Y.S.; Writing—original draft: G.E., A.M.M., S.D. and M.A.-S.; Writing—review and editing: G.E., A.M.M., M.A.-S. and S.D.; Visualization: G.E., A.M.M. and M.A.-S.; Supervision: G.E., I.V.M., G.Y.S. and S.D.; Project administration, I.V.M., I.E.S., G.Y.S. and S.D.; Funding acquisition: I.V.M., G.Y.S. and S.D. All authors have read and agreed to the published version of the manuscript.

Funding: The research was supported by the program of the National Research Tomsk Polytechnic University (Priority-2030-EEZC-031-090-2026).

Data Availability Statement: The authors do not have permission to share the data publicly.

Conflicts of Interest: The authors confirm that they have no known conflicts of interest regarding the information provided in this study, nor have they received any financial support for this work that has influenced its content in any way.

Nomenclature

The following abbreviations are used in this manuscript:

AHM	Assisted/Automated History Matching
AI	Artificial Intelligence
$F_{con.(23)}$ and $F_{con.(34)}$	Fault №23 and fault №34 conductivity
FWL	Free Water Level Depth
GOF	Global Objective Function
HM	History Matching
K (J1) Well (1)-R	Permeability Parameter of the J1 Formation Within the Voronoi Region of Well 1
K (J1) Well (3)-R	Permeability Parameter of the J1 Formation Within the Voronoi Region of Well 3
K (J1) Well (4)-R	The Permeability Parameter of the J1 Formation Within the Voronoi Region of Well 4
K_A	Coefficient "a" In the Exponential Porosity–Permeability Equation
K_B	Coefficient "b" In the Exponential Porosity–Permeability Equation
KROLW	Relative Phase Permeability of Oil with Residual Water Saturation
KRORW	The Relative Phase Permeability of Oil with Critical Water Saturation
$K_{rw}_S_{orw}$	Water Relative Permeability at Residual Oil Saturation
KRWR	Relative Phase Permeability of Water with Residual Oil Saturation
KRWR Well (1) to KRWU Well (8).	Relative Phase Permeability of Water with Residual Oil Saturation in Well 1 to Well 8 Voronoi region
KRWU Well (8), etc.	Relative Phase Permeability of Water with maximum water saturation in Well 8 Voronoi region
K_v/K_h	Vertical Permeability Anisotropy Coefficient
K_v/K_h (J1) and (J2)	Vertical permeability anisotropy multiplier in the J1 and J2 formations
K_x/K_y	Permeability Anisotropy Coefficient in XY Direction
ML	Machine Learning
N_o	Corey Exponent of Relative Permeability for Oil
NTG	Net-To-Gross
N_w	Corey Exponent of Relative Permeability for Water
OF	Objective Function
PSO	Particle Swarm Optimization
RSM	Reservoir Simulation Model
SHAP	Shapley Additive Explanations
STD	Standard Deviation
SOWCR	Residual Oil Saturation
SR	Siberian Reference Field
SRM	Synthetic Reservoir Model
SW_A	First Coefficient in The Natural Logarithmic Water Saturation-J-Function Equation
SWCR	Critical Water Saturation
SWL	Irreducible Water Saturation

SWN Well (1)-L	Normalized Water Saturation Marginal Parameter Within the Voronoi Region of Well 1
SWN Well (5)-R	Normalized Water Saturation Marginal Parameter Within the Voronoi Region of Well 5
SWN Well (6)-R	Normalized Water Saturation Marginal Parameter Within the Voronoi Region of Well 6
SWN Well (7)-L	Normalized Water Saturation Marginal Parameter Within the Voronoi Region of Well 7
TOP_J1_STD_M	Parameter for Varying the Position of the J1 Formation Top
WF	Workflow
$\sigma \cdot (\cos(t))$	Effective Component of Phase Surface Tension
φ_m	Porosity Configuration Coefficient

References

1. Davoodi, S.; Makarov, N.; Wood, D.A.; Al-Shargabi, M.; Vanovskiy, V.; Koroteev, D.; Rukavishnikov, V.S.; Burnaev, E. A Review of Artificial Intelligence Techniques Applied to Subsurface Oil and Gas Reservoir Simulation. *Appl. Soft Comput.* **2026**, *198*, 115222. [CrossRef]
2. Ning, X.; Cao, S.; Sun, H.; Yang, C.; Yuan, Y.; Wang, H. A Comprehensive Review of Optimization Algorithms in Oil and Gas Fields: Approaches and Applications. *Int. J. Commun. Syst.* **2026**, *39*, e70319. [CrossRef]
3. Reservoir Analysis Market Report 2025. Available online: https://www.researchandmarkets.com/reports/5940014/reservoir-analysis-market-report?srsltid=AfmBOopN3IoYVbTi3rnjKZ-tx-qTjoN7SFmHNVW7HU-GxCPdE3LFrUN6 (accessed on 26 January 2026).
4. Motaei, E.; Ganat, T.; Tabatabai, M.; Umer, M.; Krishna, S. Advancements in Machine Learning–Driven Proxy Modelling Techniques for Reservoir Engineering: A Systematic Review. *J. Pet. Geol.* **2026**, *49*, 516–540. [CrossRef]
5. Liu, Y.; Wu, J.; Zhang, B.; Li, C.; Zhang, D.; Wang, T.; Yang, C.; Luo, Y.; Gu, Y.; Zhang, L.; et al. An Intelligent Evaluation Method for Sweet Spots in Deep-Marine Shale Reservoirs Based on Lithofacies Control and Multi-Parameter Driving. *Processes* **2026**, *14*, 1007. [CrossRef]
6. Askarinezhad, R.; Helland, J.O.; Zuta, J.C. Automated History Matching of Steady-State CO2/Brine Drainage Experiments at Reservoir Conditions. In *Proceedings of the SPE Europe Subsurface Conference, Bergen, Norway, 21 April 2026*; SPE: Bergen, Norway, 2026.
7. Mohamed, L.M.Y. Novel Sampling Techniques for Reservoir History Matching Optimisation and Uncertainty Quantification in Flow Prediction. Ph.D. Thesis, Heriot-Watt University, Edinburgh, UK, 2011.
8. Eremyan, G.A.; Davoodi, S.; Rukavishnikov, V.S.; Stepiko, A.V. Comprehensive Approach to Parametrization of a Petroleum Reservoir Model for Automated History Matching. *Bull. Tomsk. Polytech. Univ. Geo Assets Eng.* **2021**, *332*, 138–147.
9. Temizel, C.; Tutun, S.; Canbaz, C.H.; Alagoz, E.; Dündar, E.C.; Sari, M.M.; Saputelli, L.; Oskay, M.M. AI Applications in Reservoir Characterization, Geology, and Geophysics. In *Artificial Intelligence in the Energy Industry*; CRC Press: Boca Raton, FL, USA, 2026; pp. 81–159.
10. Matveev, I.; Shishaev, G.; Eremyan, G.; Demyanov, V.; Popova, O.; Kaygorodov, S.; Belozerov, B.; Uzhegova, I.; Konoshonkin, D.; Korovin, M. Geology Driven History Matching. In Proceedings of the SPE Russian Petroleum Technology Conference, Moscow, Russia, 22–24 October 2019.
11. Liu, J.; Zhu, Y.; Liu, J.; Pan, H.; Zhang, D.; Bai, J.; Kuang, T.; Sun, T. A Novel Physics-Based Subsidiary Fracture Networks Grading and Permeability Equivalence for Efficient Shale Reservoir Simulation in History Matching. *SPE J.* **2026**, *31*, 497–519. [CrossRef]
12. Nazirova, E.; Nematov, A.; Artikbaeva, G.; Ismailov, S.; Shukurova, M.; Nematov, A.R.; Matyakubov, M. Mathematical Modeling of Pressure-Dependent Variation in the Hydrodynamic Parameters of Gas Fields. *Modelling* **2026**, *7*, 30. [CrossRef]
13. Bhattacharyya, S.; Vyas, A. Machine-Learning Application for Fast 3-Phase Black Oil Reservoir Simulation. *J. Energy Eng.* **2026**, *152*, 4026002. [CrossRef]
14. Barrela, E.; Demyanov, V.; Azevedo, L. Coupling Geologically Consistent Geostatistical History Matching with Parameter Uncertainty Quantification. *arXiv* **2018**, arXiv:1810.06642. [CrossRef]
15. Zhao, Y.; Luo, R.; Li, L.; Zhang, R.; Zhang, D.; Zhang, T.; Xie, Z.; Luo, S.; Zhang, L. A Review on Optimization Algorithms and Surrogate Models for Reservoir Automatic History Matching. *Geoenergy Sci. Eng.* **2024**, *233*, 212554. [CrossRef]
16. Liu, P.; Zhang, K.; Yao, J. Reservoir Automatic History Matching: Methods, Challenges, and Future Directions. *Adv. Geoenergy Res.* **2023**, *7*, 136–140. [CrossRef]
17. Ndubuka, C.I.; Ita, O.E. History Matching in a Reservoir Model Using an Automatic Approach. *J. Eng. Res. Rep.* **2024**, *26*, 371–387. [CrossRef]

18. Daoud, M.S.; Shehab, M.; Al-Mimi, H.M.; Abualigah, L.; Zitar, R.A.; Shambour, M.K.Y. Gradient-Based Optimizer (GBO): A Review, Theory, Variants, and Applications. *Arch. Comput. Methods Eng.* **2023**, *30*, 2431–2449. [CrossRef]
19. Arroyo Negrete, E.; Rodiguez, J.; Goryachev, S.; Belova, N.; Al Blooshi, A.; Basioni, M. Automatic History Matching Theory, Implementation, and Field Applications. In Proceedings of the Abu Dhabi International Petroleum Exhibition & Conference, Abu Dhabi, United Arab Emirates, 12–15 November 2018.
20. Wang, L.; Yao, Y.; Luo, X.; Daniel Adenutsi, C.; Zhao, G.; Lai, F. A Critical Review on Intelligent Optimization Algorithms and Surrogate Models for Conventional and Unconventional Reservoir Production Optimization. *Fuel* **2023**, *350*, 128826. [CrossRef]
21. Sanghyun, L.; Stephen, K.D. Optimizing Automatic History Matching for Field Application Using Genetic Algorithm and Particle Swarm Optimization. In Proceedings of the OTC, Kuala Lumpur, Malaysia, 20–23 March 2018.
22. Vazquez, O.; Young, C.; Demyanov, V.; Arnold, D.; Fisher, A.; MacMillan, A.; Christie, M. Produced-Water-Chemistry History Matching in the Janice Field. *SPE Reserv. Eval. Eng.* **2015**, *18*, 564–576. [CrossRef]
23. Rostamian, A.; de Moraes, M.B.; Schiozer, D.J.; Coelho, G.P. A Survey on Multi-Objective, Model-Based, Oil and Gas Field Development Optimization: Current Status and Future Directions. *Pet. Sci.* **2025**, *22*, 508–526. [CrossRef]
24. Shams, M.; El-Banbi, A.H.; Sayyouh, H. A Novel Assisted History Matching Workflow and Its Application in a Full Field Reservoir Simulation Model. *J. Pet. Sci. Technol.* **2019**, *9*, 64–87.
25. Mohamed, L.; Christie, M.; Demyanov, V.; Robert, E.; Kachuma, D. Application of Particle Swarms for History Matching in the Brugge Reservoir. In Proceedings of the SPE Annual Technical Conference and Exhibition, Florence, Italy, 19–22 September 2010.
26. Louhichi, M.; Nesmaoui, R.; Mbarek, M.; Lazaar, M. Shapley Values for Explaining the Black Box Nature of Machine Learning Model Clustering. *Procedia Comput. Sci.* **2023**, *220*, 806–811. [CrossRef]
27. Karim, F.; Armin, M.A.; Ahmedt-Aristizabal, D.; Tychsen-Smith, L.; Petersson, L. A Review of Hydrodynamic and Machine Learning Approaches for Flood Inundation Modeling. *Water* **2023**, *15*, 566. [CrossRef]
28. Hancock, J.T.; Khoshgoftaar, T.M. CatBoost for Big Data: An Interdisciplinary Review. *J. Big Data* **2020**, *7*, 94. [CrossRef] [PubMed]
29. Morozov, A.D.; Popkov, D.O.; Duplyakov, V.M.; Mutalova, R.F.; Osiptsov, A.A.; Vainshtein, A.L.; Burnaev, E.V.; Shel, E.V.; Paderin, G.V. Data-Driven Model for Hydraulic Fracturing Design Optimization: Focus on Building Digital Database and Production Forecast. *J. Pet. Sci. Eng.* **2020**, *194*, 107504. [CrossRef]
30. Tang, J.; Fan, B.; Xiao, L.; Tian, S.; Zhang, F.; Zhang, L.; Weitz, D. A New Ensemble Machine-Learning Framework for Searching Sweet Spots in Shale Reservoirs. *SPE J.* **2021**, *26*, 482–497. [CrossRef]
31. Tang, J.; Fan, B.; Xu, G.; Xiao, L.; Tian, S.; Luo, S.; Weitz, D. A New Tool for Searching Sweet Spots by Using Gradient Boosting Decision Trees and Generative Adversarial Networks. In Proceedings of the International Petroleum Technology Conference, IPTC, Dhahran, Saudi Arabia, 13–15 January 2020.
32. Shapley, L.S. 17. A Value for n-Person Games. In *Contributions to the Theory of Games (AM-28), Volume II*; Kuhn, H.W., Tucker, A.W., Eds.; Princeton University Press: Princeton, NJ, USA, 1953; pp. 307–318.
33. Lundberg, S.; Lundberg, S.M.; Allen, P.G.; Lee, S.-I. A Unified Approach to Interpreting Model Predictions. *arXiv* **2017**, arXiv:1705.07874. [CrossRef]
34. Kan, Z.; Chen, B.; Yu, W.; Chen, S.; Chen, G. Risk Identification of Mangroves Facing Spartina Alterniflora Invasion Using Data-Driven Approaches with UAV and Machine Learning Models. *Remote Sens. Environ.* **2025**, *319*, 114613. [CrossRef]
35. Eremyan, G.; Matveev, I.; Shishaev, G.; Rukavishnikov, V.; Demyanov, V. How Does the Definition of the Objective Function Influence the Outcome of History Matching? In *Proceedings of the ECMOR XVII*; European Association of Geoscientists & Engineers: Kosterijland, The Netherlands, 2020.
36. Jansen, J.D.; Fonseca, R.M.; Kahrobaei, S.; Siraj, M.M.; Van Essen, G.M.; Van den Hof, P.M.J. The Egg Model—A Geological Ensemble for Reservoir Simulation. *Geosci. Data J.* **2014**, *1*, 192–195. [CrossRef]
37. Khan, M.; Nawaz, S.; Gao, X.; Khan, N.M. Reservoir Characterization of Eocene Carbonates and Cambrian Sands in the Eastern Potwar Region, Pakistan. *Reserv. Sci.* **2026**, *2*, 111–125. [CrossRef]
38. Tian, L.; Zhang, Q.; Li, X.; Li, C. Fracturing Effectiveness Evaluation Based on Flowback Data Using Pressure Transient Testing. *Reserv. Sci.* **2026**, *2*, 97–110. [CrossRef]
39. Ali, J.; Ansari, U.; Ali, F.; Javed, T.; Hullio, I.A. Application of Machine Learning for Effective Screening of Enhanced Oil Recovery Methods. *Reserv. Sci.* **2026**, *2*, 65–80. [CrossRef]
40. Hutahaean, J.J.; Demyanov, V.; Christie, M.A. Impact of Model Parameterisation and Objective Choices on Assisted History Matching and Reservoir Forecasting. In Proceedings of the SPE/IATMI Asia Pacific Oil & Gas Conference and Exhibition, Nusa Dua, Indonesia, 20–22 October 2015.
41. Bertolini, A.C.; Schiozer, D.J. Influence of the Objective Function in the History Matching Process. *J. Pet. Sci. Eng.* **2011**, *78*, 32–41. [CrossRef]
42. Eremyan, G.A. Selection of an Objective Function for Solving the Problem of Automated History Matching of a Reservoir Simulation Model: Dissertation for the Degree of Candidate of Technical Sciences: Specialty 2.3.1. Ph.D Thesis, Tomsk Polytechnic University, Tomsk, Russia, 2022.

43. Sulaksana, A.; Thiam, F.; Tan, L.-H.; Garimela, V.S.S. Practical Application of Experimental Design ED to Improve Deterministic History Matching and Manage Uncertainty in Mature Waterflood Field Development. In Proceedings of the IPTC, Bangkok, Thailand, 12 November 2016.
44. Torres, K.M.; Al Hashmi, N.F.; Al Hosani, I.A.; Al Rawahi, A.S.; Parra, H. Reducing the Uncertainty of Static Reservoir Model in a Carbonate Platform, through the Implementation of an Integrated Workflow: Case A-Field, Abu Dhabi, UAE. In Proceedings of the Abu Dhabi International Petroleum Exhibition & Conference, Abu Dhabi, United Arab Emirates, 7–10 November 2016.
45. He, W.; Li, X.; Wan, Y.; Zhan, H.; Wan, N.; He, S.; Lin, Y.; Wang, L.; Yu, W.; Chen, L. EUR Prediction for Shale Gas Wells Based on the ROA-CatBoost-AM Model. *Appl. Sci.* **2025**, *15*, 2156. [CrossRef]
46. Ostroumova, L.; Gusev, G.; Vorobev, A.; Dorogush, A.V.; Gulin, A. CatBoost: Unbiased Boosting with Categorical Features. *Neural Inf. Process. Syst.* **2017**, *31*, 6639–6649.
47. Mckay, M.D.; Beckman, R.J.; Conover, W.J. A Comparison of Three Methods for Selecting Values of Input Variables in the Analysis of Output from a Computer Code. *Technometrics* **2000**, *42*, 55–61. [CrossRef]
48. Helton, J.C.; Davis, F.J. Latin Hypercube Sampling and the Propagation of Uncertainty in Analyses of Complex Systems. *Reliab. Eng. Syst. Saf.* **2003**, *81*, 23–69. [CrossRef]
49. Esfandi, T.; Sadeghnejad, S.; Jafari, A. Effect of Reservoir Heterogeneity on Well Placement Prediction in CO_2-EOR Projects Using Machine Learning Surrogate Models: Benchmarking of Boosting-Based Algorithms. *Geoenergy Sci. Eng.* **2024**, *233*, 212564. [CrossRef]
50. Lundberg, S.M.; Erion, G.; Chen, H.; DeGrave, A.; Prutkin, J.M.; Nair, B.; Katz, R.; Himmelfarb, J.; Bansal, N.; Lee, S.-I. From Local Explanations to Global Understanding with Explainable AI for Trees. *Nat. Mach. Intell.* **2020**, *2*, 56–67. [CrossRef]
51. Shapley, L.S. A Value for *n*-Person Games. In *The Shapley Value*; Roth, A.E., Ed.; Cambridge University Press: Cambridge, UK, 1988; pp. 31–40.
52. Shi, Y.; Zhong, W.; Peng, X.; Yang, M.; Du, W. Interpretable Reconstruction of Naphtha Components Using Property-Based Extreme Gradient Boosting and Compositional-Weighted Shapley Additive Explanation Values. *Chem. Eng. Sci.* **2024**, *284*, 119462. [CrossRef]
53. Cremades, A.; Hoyas, S.; Vinuesa, R. Additive-Feature-Attribution Methods: A Review on Explainable Artificial Intelligence for Fluid Dynamics and Heat Transfer. *Int. J. Heat Fluid Flow* **2024**, *9*, 109662. [CrossRef]
54. Yao, Y.; Qiu, Y.; Cui, Y.; Wei, M.; Bai, B. Insights to Surfactant Huff-Puff Design in Carbonate Reservoirs Based on Machine Learning Modeling. *Chem. Eng. J.* **2023**, *451*, 138022. [CrossRef]
55. Wen, S.; Wei, B.; You, J.; He, Y.; Ye, Q.; Lu, J. Rapid Screening and Optimization of CO_2 Enhanced Oil Recovery Operations in Unconventional Reservoirs: A Case Study. *Petroleum* **2025**, *11*, 188–200. [CrossRef]
56. Eberhart, R.; Kennedy, J. A New Optimizer Using Particle Swarm Theory. In *Proceedings of the MHS'95. Proceedings of the Sixth International Symposium on Micro Machine and Human Science*; IEEE: Piscataway, NJ, USA, 2002.
57. Dabiri, M.-S.; Haji-Hashemi, R.; Ashoorian, S.; Schaffie, M.; Zabihi, R.; Hemmati-Sarapardeh, A. Modeling Drilling Fluid Density at High-Pressure High-Temperature Conditions Using Advanced Machine-Learning Techniques. *Geoenergy Sci. Eng.* **2025**, *244*, 213369. [CrossRef]
58. Yusup, N.; Zain, A.M.; Hashim, S.Z.M. Overview of PSO for Optimizing Process Parameters of Machining. *Procedia Eng.* **2012**, *29*, 914–923. [CrossRef]
59. Gad, A.G. Particle Swarm Optimization Algorithm and Its Applications: A Systematic Review. *Arch. Comput. Methods Eng.* **2022**, *29*, 2531–2561. [CrossRef]
60. Delavar, M.R.; Ramezanzadeh, A.; Gholami, R.; Sanei, M. Optimization of Drilling Parameters Using Combined Multi-Objective Method and Presenting a Practical Factor. *Comput. Geosci.* **2023**, *175*, 105359. [CrossRef]
61. Zounemat-Kermani, M.; Batelaan, O.; Fadaee, M.; Hinkelmann, R. Ensemble Machine Learning Paradigms in Hydrology: A Review. *J. Hydrol.* **2021**, *598*, 126266. [CrossRef]
62. Anemangely, M.; Ramezanzadeh, A.; Tokhmechi, B.; Molaghab, A.; Mohammadian, A. Drilling Rate Prediction from Petrophysical Logs and Mud Logging Data Using an Optimized Multilayer Perceptron Neural Network. *J. Geophys. Eng.* **2018**, *15*, 1146–1159. [CrossRef]
63. Xu, W.S.; Luo, P.Y.; Sun, L.; Lin, N. A Prediction Model of the Capillary Pressure J-Function. *PLoS ONE* **2016**, *11*, e0162123. [CrossRef]
64. Adetosoye, A.A.; Moreno, J.J.; Al Ghuzaily, M.A.; Ulincy, A.J.; Urazimanova, A.M.; Samad, A.; Barroeta, R.G.; Portilla, C.A. Log Derived Novel Approach to Estimate Vertical Permeability in Multilayer Reservoirs through Resistivity Anisotropy in the Natih Formation, Oman. In Proceedings of the Abu Dhabi International Petroleum Exhibition & Conference (ADIPEC), Abu Dhabi, United Arab Emirates, 2–5 October 2023.
65. Yuan, H.; Liu, M.; Kang, L.; Miao, C.; Wu, Y. An Empirical Study of the Effect of Background Data Size on the Stability of SHapley Additive exPlanations (SHAP) for Deep Learning Models. *arXiv* **2022**, arXiv:2204.11351.

66. Gebreyesus, Y.; Dalton, D.; Nixon, S.; De Chiara, D.; Chinnici, M. Machine Learning for Data Center Optimizations: Feature Selection Using Shapley Additive exPlanation (SHAP). *Future Internet* **2023**, *15*, 88. [CrossRef]
67. Rios, V.S.; Santos, L.O.S.; Schiozer, D.J. Upscaling Technique for Highly Heterogeneous Reservoirs Based on Flow and Storage Capacity and the Lorenz Coefficient. *SPE J.* **2020**, *25*, 1981–1999. [CrossRef]
68. You, J.; Ampomah, W.; Kutsienyo, E.J.; Sun, Q.; Balch, R.S.; Aggrey, W.N.; Cather, M. Assessment of Enhanced Oil Recovery and CO2 Storage Capacity Using Machine Learning and Optimization Framework. In Proceedings of the SPE Europec featured at 81st EAGE Conference and Exhibition, London, UK, 3–6 June 2019.
69. Fu, J.; Chen, H.; Yao, C.; Sakaida, S.; Kerr, E.; Johnson, A.; Datta-Gupta, A.; Zhu, D.; Hill, A.D. Field Application of a Novel Multiresolution Multiwell Unconventional Reservoir Simulation: History Matching and Parameter Identification. *SPE J.* **2024**, *29*, 2703–2714. [CrossRef]
70. Kochnev, A.; Kozyrev, N.; Krivoshchekov, S. Estimation of the Influence of Fracture Parameters Uncertainty on the Dynamics of Technological Development Indicators of the Tournaisian-Famennian Oil Reservoir in Sukharev Oil Field. *J. Min. Inst.* **2022**, *258*, 1026–1037. [CrossRef]

Disclaimer/Publisher's Note: The statements, opinions and data contained in all publications are solely those of the individual author(s) and contributor(s) and not of MDPI and/or the editor(s). MDPI and/or the editor(s) disclaim responsibility for any injury to people or property resulting from any ideas, methods, instructions or products referred to in the content.